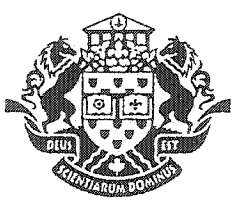

Université d'Ottawa · University of Ottawa

Université d'Ottawa · University of Ottawa

FACULTÉ DES ÉTUDES SUPÉRIEURES ET POSTDOCTORALES

FACULTY OF GRADUATE AND POSTDOCTORAL STUDIES

Luc CHARRON

AUTEUR DE LA THÈSE - AUTHOR OF THESIS

M. Sc. (Physics)

GRADE - DEGREE

Department of Physics

FACULTÉ, ÉCOLE, DÉPARTEMENT - FACULTY, SCHOOL, DEPARTMENT

TITRE DE LA THÈSE - TITLE OF THE THESIS

Radiative Properties of MoS2 and Other Transition Metal Dichalcogenides

E. Fortin

DIRECTEUR DE LA THÈSE - THESIS SUPERVISOR

CO-DIRECTEUR DE LA THÈSE - THESIS CO-SUPERVISOR

EXAMINATEURS DE LA THÈSE - THESIS EXAMINERS

J. Armitage

P. Piercy

A. Song

J.-M. De Koninck, Ph.D.

LE DOYEN DE LA FACULTÉ DES ÉTUDES SUPÉRIEURES ET POSTDOCTORALES

DEAN OF THE FACULTY OF GRADUATE AND POSTDOCTORAL STUDIES

Radiative properties of MoS_2 and other transition metal dichalcogenides

By

©Luc G. Charron

Thesis submitted to the
Faculty of Graduate and Postdoctoral Studies
in partial fulfillment of the requirements
for the degree of Master of Science in Physics

Department of Physics

University of Ottawa
Ottawa, Ontario
April 26, 2004

Your file Votre référence
ISBN: 0-494-01434-2
Our file Notre référence
ISBN: 0-494-01434-2

Abstract

Low temperature radiative properties of the layered transition metal dichalcogenides 2H-MoS_2, 2H-WS_2 and 2H-WSe_2 are investigated. Synthetically grown crystals of all three materials, natural 2H-MoS_2 single crystals and several 2H-MoS_2 and 2H-WS_2 commercial powders are studied. Steady-state photoluminescence(PL) measurements performed on the samples reveal two distinct radiative regions in the near infrared. The first region consisting of several sharp lines is produced by bound excitons related to the halogen transport agent intercalated within the van der Waals gap of the layered compounds. The second weaker region, composed of a broad spectral band, originates from the radiative recombination between an intrinsic crystal lattice defect center and the valence band in the conditions of a strong electron-phonon coupling. Time decay analysis of the bound excitonic radiative transitions is performed with time-resolved and PL intensity ratio measurements. The spectral and temperature dependence of the total radiative emissions of all three compounds are described in the framework of a two-channel kinetic recombination model in thermal equilibrium conditions. A configuration coordinate diagram is also constructed for 2H-MoS_2. PL intensity measurements performed on the 2H-MoS_2 and 2H-WS_2 synthetic crystals reveal a sublinear PL dependence on excitation intensity. Finally a technique developed to intercalate halogen molecules in natural 2H-MoS_2 single crystals is described.

Sommaire

Les propriétés radiatives des métaux de transitions dichalcogénides à couches 2H-MoS_2, 2H-WS_2 et 2H-WSe_2 se produisant à basses températures sont examinées. Des cristaux synthétiques des trois composés, des cristaux naturels de 2H-MoS_2 ainsi que plusieurs poudres commerciales de 2H-MoS_2 et de 2H-WS_2 sont étudiés. Les mesures de photoluminescence (PL) auprès des échantillons révélent deux régions radiatives distinctes. La première région consiste de plusieurs lignes fines et serait produite par des excitons liés reliés aux molécules halogènes intercalées à l'intérieur du gap de van der Waals des matériaux. La deuxième région, plus faible que la première, comprend une bande spectrale très large provenant des recombinaisons radiatives entre des centres de défauts intrinsèques du réseau cristallin et de la bande de valence lors d'un couplage électron-phonon fort. Une analyse des durées de vie aux transitions radiatives des excitons liés est effectuée grâce aux mesures de temps radiatifs ainsi que des mesures de rapports d'intensité. La dépendence spectrale et en température des émissions radiatives totales des trois composés sont décrites l'aide d'un modèle cinétique de recombinaison à deux canaux en équilibre thermique. Un diagramme de configuration pour le 2H-MoS_2 est aussi construit. Des mesures d'intensité effectuées sur les cristaux synthétiques de 2H-MoS_2 et de 2H-WS_2 révélent une relation sous-linaire de la PL en fonction de l'intensité d'excitation. Finalement, une technique d'intercalation d'halogènes à l'intérieure des cristaux naturels de 2H-MoS_2 est décrite.

Remerciements

J'aimerais d'abords remercier Dr. Emery Fortin pour son aide et son encouragement tout au long de ce projet. J'aimerais également remercier le Dr. Léonid Kulyuk et le Dr. Sylvain Raymond pour leur importante collaboration avec certaines mesures et calculs théoriques. Je remercie Pierre Leblanc pour son aide au laboratoire et son encouragement ainsi que Hervé Beaudoin et toute l'équipe à l'atelier d'usinage pour leur aide. Je remercie Stephanie Linney pour sa présence et son support. Finalement, je remercie mon père Michel et ma mère Claire, sans qui je n'aurais pu compléter mes études avec autant de succès.

Statement of Originality

Unless indicated otherwise, experimental results on the 2H-MoS_2 and 2H-WS_2 presented in this thesis were collected by the author during experiments at the University of Ottawa or at the National Research Council (NRC) in Ottawa in collaboration with Dr. S. Raymond. The measurements on the 2H-WSe_2 were performed at the University of Konstanz, Germany by Dr. Kulyuk.

Some of the results shown in this thesis were (or will be) presented in the following:

Conference Proceedings

- Bound Excitonic Luminescence of the Intercalated Tungsten Dichalcogenide Layer Compounds, 5th International Conference Excitonic Processes in Condensed Matter (EXCON 2002), L. Kulyuk, E. Bucher, L. Charron, E. Fortin, A. Nateprov, O. Schenker, Darwin, Australia, July 2002.

- Photoluminescence in 2H-WS_2, L. Charron, L. Kulyuk, and E. Fortin, Canadian Association of Physicists (CAP) Congress, Quebec City, June 2002.

- Photoluminescence in Molybdenite, L. Charron, L. Kulyuk, E. Fortin and Y. Braik, Canadian Association of Physicists (CAP) Congress, Charlottetown (PEI), June 2003.

- Photoluminescence in 2H-MoS_2, L. Charron, L. Kulyuk, E. Fortin, Y. Braik, Annual APS March Meeting, Montréal 2004.

- Radiative Recombination of Excitons in the Transition-Metal Dichalcogenides MoS_2:Cl_2 and WS_2:Br_2, L. Charron, D. Dumchenko, E. Fortin, C. Gherman, L. Kulyuk, 27th International Conference of Physics of Semiconductors, Flagstaff, Arizona, July 2004.

- Radiative Processes in Layered Transition Metal Dichalcogenides: The Role of the Halogen Molecules Intercalation, L. Kulyuk, E. Bucher, L. Charron, D. Dumchenko, E. Fortin, C. Gherman, 6th International Conference on Excitonic Processes in Condensed Matter(EXCON 2004), Poland, July 2004.

Journal Papers

- Bound exciton luminescence of the intercalated tungsten dichalcogenide layer compounds, L. Kulyuk, E. Bucher, L. Charron, E. Fortin, A. Nateprov, O. Schenker, Journal of Nonlinear Optics, 29(7-9), 501 (2002).

- Radiative properties of MoS_2 layered crystals, L. Kulyuk, L. Charron, E. Fortin, Phys. Rev. B 68, 075314 (2003)

- Radiative properties of the intercalated MoS_2:Cl_2 layered crystals, D. Dumchenko, C. Gherman, L. Charron, E. Fortin, L. Kulyuk, Semiconductor Conference, CAS 2003 (IEEE), Vol. 2, 314 (2003)

Contents

List of Figures

List of Tables

Introduction

The semiconductor and optoelectronic industry is well established and has flourished for over 50 years. The ever-increasing demand for progressively more efficient and accurate optoelectronic devices required the conception of novel materials with useful and interesting properties. New semiconductors are constantly being created by means of crystal growth techniques and doping existing materials with various impurities. Aside from silicon, germanium and the III-V compounds which are still clearly the current dominant semiconductors, transition metal dichalcogenides have also been the subject of extensive investigation of their optical, electrical and structural properties [1, 2, 3].

The layered transition metal dichalcogenide (TX_2) semiconductors are an interesting class of material due to their quasi-two-dimensional crystallographic structure consisting of covalently bonded X-T-X sheets linked by weak van der Waals forces. The 2H (Hexagonal) polytype Molybdenum and tungsten disulphide (2H-MoS_2 and 2H-WS_2) as well as tungsten diselenide (2H-WSe_2) are three of such layered semiconductors which have been studied in great detail. All three materials crystallize in the hexagonal structure belonging to the space group $P6_3/mmc - D^4_{6h}$ and like all TX_2 compounds they are indirect band gap semiconductors [4, 5, 6]. 2H-MoS_2 , 2H-WS_2 and 2H-WSe_2 have been considered for electrochemical and solid state solar cell applications because of the close correspondence between their optical band gap and the solar spectrum [7, 8]. 2H-MoS_2 and 2H-WS_2 compounds are also of great interest in nanotechnology since they were the first to be synthesized as inorganic fullerene-like nanotubes [9, 10, 11].

One of the most interesting aspects of the layered semiconductor is its capability of intercalating impurities between the X-T-X sheets due to the weak nature of the van der Waals binding energy. Various metal and ion intercalation processes and their effects on layered transition metal dichalcogenides have been very well documented [12, 13, 14, 15, 16, 17, 18]. Intercalation not only alters existing solid state properties of the materials but also creates new ones. Radiative properties of 2H-MoS_2, 2H-WS_2 and 2H-WSe_2 caused by the intercalation of halogen molecules were observed for the first time by the

author and his collaborators [19, 20].

The objective of this thesis is to document and explain the newly discovered optical properties of the layered transition metal dichalcogenides as well as the intercalation process of the halogen impurities. Despite the numerous publications on optical studies, photoluminescence of 2H-MoS_2 and other layered semiconductors has never been documented. The lack of infrared detectors available when the layered compounds were first investigated could explain the optical phenomenon's oversight. This research shall focus on the 2H-MoS_2 semiconductor since it is an abundant material which can be found in nature as molybdenite and can also be synthetically grown. The 2H-WS_2 and 2H-WSe_2 compounds shall also be studied in order to illustrate that the radiative properties observed in the layered compounds are general phenomenona occurring in several transition metal dichalcogenides. In addition to the synthetic and natural single crystals, commercial MoS_2 and WS_2 powders will also be analyzed.

The radiative emission observed in the investigated compounds is located in the near infrared between 0.7 and 1.35 eV. Two distinct radiative regions were identified. The first photoluminescence(PL) region was centered at 1.18 eV for the MoS_2 and WSe_2 and 1.32 eV in the WS_2 samples. Consisting of sharp excitonic lines and their phonon replicas, the emissions of the first regions have been attributed to the recombination of bound excitons related to the transport agent intercalated in the materials during the growth process. The diatomic halogen molecules, chlorine for MoS_2 and bromine or iodine for WS_2 and WSe_2, positioned between the layers give rise to neutral centers, providing efficient radiative emissions in indirect semiconductors. The second weaker region composed of a broad spectral band centered at 0.95, 0.97 and 0.83 eV for MoS_2, WS_2 and WSe_2 respectively, was observed for all types of samples, including the natural molybdenite, and has been ascribed to radiative recombinations from deep donor centers caused by intrinsic lattice defects. It was initially believed that the PL of the excitonic region was inherent to synthetic single crystals, where the halogen impurities were intercalated during the VTM (vapor transport method) growth process, since no excitonic PL was observed in the naturally occurring single crystals. However, experiments on commercial natural 2H-MoS_2 powders revealed similar radiative properties to those in the synthetic single crystals, suggesting the intercalation of halogen molecules can also be achieved by other methods than during the growth process.

Three types of PL measurements, steady-state PL, time-resolved and intensity dependent PL are reported in this thesis. PL spectra for every samples were obtained with steady-state PL measurements at different temperatures (2K-150K) and were used to

investigate the spectral shape and temperature dependence of the radiative emissions. Time-resolved measurements were also performed on synthetic 2H-WS_2 to characterize the radiative recombination processes by which the electrons decay. Finally a preliminary study on the PL intensity dependence was performed on some MoS_2 and WS_2 samples. Several geometrical lattice calculations and successful photoconductivity(PC) measurements of the synthetic molybdenum and tungsten disulphide single crystals were also carried out to provide further insight on the origins of the radiative properties in the materials. The results from the time-resolved and steady-state PL measurements were described by a time-decay and kinetic recombination model respectively. The PL intensity dependent experimental data was described by a simple power equation. A configuration coordinate diagram (CCD) model was also constructed for the MoS_2 single crystal. Finally, a technique was devised to intercalate halogen molecules in natural MoS_2 single crystals.

The thesis is divided into three chapters. The first introduces briefly but adequately some theoretical concepts necessary for the analysis of the optical phenomenon at hand. This includes a short introduction on band structures, excitons, phonons, thermal quenching and photoconductivity. The models and the configuration coordinate diagram are also presented in this chapter. The second chapter presents the samples and their preparation, the experimental techniques, the equipment used and the halogen intercalation method performed on the natural MoS_2 single crystals. The third and final chapter will present the results obtained from the three types of PL measurements, apply the models introduced in the first chapter to the experimental data, construct the CCD for the MoS_2 compound and discuss the halogen intercalation of natural MoS_2 single crystals.

Chapter 1

Theory

This chapter will present the theoretical background needed to describe the observed photoluminescence of the transition metal dichalcogenides. The first section includes a brief overview of some fundamental concepts of semiconductor theory. Section 1.2 will deal with optical transitions and selection rules and will serve as an introduction to the following section(1.3): photoluminescence in solids. That section will present the basic notions of excitons, phonons and their interactions as well as thermal quenching. Section 1.4 will present the time-decay and kinetic recombination models as well as the configuration coordinate model used to describe the experimental data in this work. Finally, a short section on photoconductivity measurements will close this chapter.

1.1 Semiconductor theory

The aim of this section is to present a brief overview of some important fundamental concepts on semiconductor theory. A qualitative description on energy bands and how they are calculated will first be presented. Then we will discuss how some of the information extracted from band structure calculations may be used to classify materials. Finally the effects of impurities in semiconductors will be treated.

1.1.1 Energy bands

Electrons in a crystal are confined to energy bands generated by the periodicity of the crystal lattice. These bands are separated by energy gaps which cannot be occupied by the electrons. Therefore the electrons are confined to the energy bands and can only move from one band to another if energy of equal or greater value than the energy

gap is given to the system. Calculation of these energy bands and gaps in a crystal is possible through a series of approximations. Crystal symmetry, defined as the invariance of the crystal structure to geometrical transformations, is an important concept used to facilitate the complex band calculations. There are many types of symmetries such as translational, rotational and reflection. Group theory is the mathematical tool used to classify wave functions in crystals that are invariant to symmetry operations. Classifying wave functions in this way leads to the creation of selection rules which are of great importance in semiconductor optics and will be further studied in section 1.2.1.

1.1.2 Classification of solids

Materials can be classified by the electronic occupation of their energy bands at low temperatures as well as their band gaps. Conduction is defined as the electron's ability to move inside energy bands under the influence of an electric field; this occurs only if a partially filled band is available. The highest filled energy band is called the valence band while the energy band just above it is called the conduction band. If the conduction band is partly filled, the material is called a metal but if it is empty, the material is classified as an insulator. An insulator with a small band gap between the valence and the conduction band is called a semiconductor. Essentially, a semiconductor is an insulator for which thermal energy is usually sufficient to promote electrons from the valence band to the conduction band, providing a weak current in the presence of an electric field.

There are two types of semiconductor band gaps: direct and indirect. In a direct gap the valence band maximum is aligned directly over the minima of the conduction band in momentum space (also known as k-space, where k represents the electron wave vector). In an indirect gap, the minima and maxima are shifted from one another (direct and indirect band gaps will be described in greater detail in section 1.2.1). The band structure of many transition metal dichalcogenide semiconductors including 2H-MoS_2, 2H-WS_2 and 2H-WSe_2 have been calculated and experimentally measured by various methods: they were shown to be indirect-gap semiconductors [4, 5, 6].

1.1.3 Impurities

Doping semiconductors with impurities will modify the energy band configuration of the crystals creating new allowed energy levels within the forbidden band gap. If the impurity replaces one of the atoms in a lattice and provides one or more additional electrons, the impurity is called a donor. On the other hand, if the impurity provides fewer electrons

than the substituted atom, it becomes an acceptor. An impurity replacing an atom in the crystal lattice of the same valence is called an isoelectronic center. The impurity can also lodge itself in an interstitial (empty space between atoms and molecules) position and not replace an atom in the lattice. In that case, the nature of the impurity will dictate if it is a donor or acceptor.

1.2 Optical transitions

Optical transitions are responsible for numerous applications of semiconductors such as lasers, light emitting diodes and photodectectors. These transitions occur between different energy levels and are achieved through various excitation and de-excitation mechanisms within the crystal.

Promoting an electron from a low to a higher energy state, generally from the valence band to the conduction band, is accomplished by absorption of an energy quanta equal to the energy difference of the final and initial states of the electron. This energy can be obtained by means of optical, thermal, electrical or any other types of excitation. The excited state of the electron caused by this energy absorption has a certain lifetime and will eventually decay back to its preferred low energy state; the ground state. This decay process emits an amount of energy once again equivalent to the energy difference between the two states of the electron. These two types of transitions produced by absorption and emission of energy are essentially the reverse of one another. Transitions involving absorption and emission of photons are appropriately called optical transitions.

1.2.1 Selection rules

Optical transitions obey selections rules which determine if a transition is allowed or forbidden. These rules are created due to conservation laws, crystal symmetry and light-matter interactions such as electric and magnetic dipole and quadrupole radiative processes. Optical transitions in direct and indirect gap semiconductor shown in Figure 1.1 (A) and (B) must obey energy and momentum conservation laws. Since the conduction band minimum is not centered over the valence band maximum, the optical transition of the indirect gap semiconductor in Figure 1.1 (B) can only be respected if the absorption of the photon is accompanied by the emission or absorption of a phonon (a quantized lattice vibration) of frequency Ω. Therefore the selection rule originating from the energy conservation law is given as:

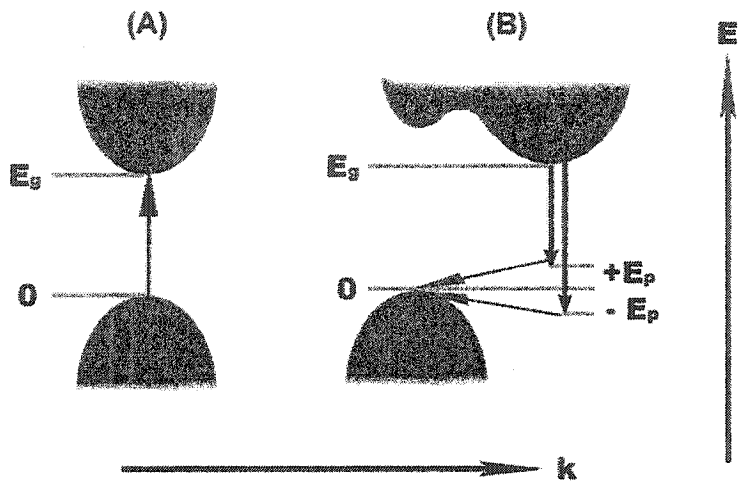

Figure 1.1: (A) Direct optical transition. (B) Indirect optical transition. E_g is the energy of the band gap and E_p is the phonon energy.

$$E_f = E_i + \hbar\omega \pm \hbar\Omega \tag{1.1}$$

where E_f and E_i are respectively the final and initial energy, $\hbar\omega$ refers to the photon energy and $\hbar\Omega$ represents the phonon energy. The selection rule from the momentum conservation law is shown to be:

$$\mathbf{k}_f = \mathbf{k}_i \pm \mathbf{K} \tag{1.2}$$

where k_f and k_i describe the final and initial electron wave vectors and K is the phonon wave vector.

As for symmetry and light-matter interaction selection rules, they are derived respectively from group theory (as stated in section 1.1.1) and quantum mechanical manipulations of radiative processes.

1.2.2 Spin-orbit coupling

Interactions between quantum components such as the spin and orbital angular momentum can lift degeneracies of certain energy levels. If the interaction between the spin (s)

and orbital momentum (l) of two particles is weak, the orbital momentums as well as the spins of both particles must first be coupled to obtain the total orbital momentum $l_1 + l_2 = L$ and the total spin $s_1 + s_2 = S$. The spin-orbit coupling can then be introduced as $J = L + S$. On the other hand, if the spin-orbit interaction is strong, the s and l must be coupled to give $j = l + s$ for each electron. Subsequently both spin-orbit interaction can then be coupled to form the jj spin-orbit coupling.

The jj coupling, observed in many semiconductors with bound excitons is often expressed as a zero-phonon doublet (labeled A and B lines). The exciton recombination from the A level is allowed while the B level transition is forbidden. Nevertheless, it is still possible to observe B radiative recombination transitions due to thermalization of the levels and to the luminescence centers' asymmetry.

1.3 Photoluminescence in solids

Luminescence occurs when an electron decays by means of an optical transition, emitting a photon. Radiative emission from solids is first achieved by exciting the crystal using various methods. For example one can excite the sample by applying a current, a process which can result in electroluminescence. Thermoluminescence is achieved when heat is used as the excitation sources while for cathodoluminescence, high-energy electrons bombard the crystal to excite it. Luminescence produced by photons with energy higher than the band gap is called photoluminescence and will be the main topic of this work.

There are two types of photoluminescence: intrinsic and extrinsic. Intrinsic photoluminescence originates from the host lattice electrons in the crystal whereas extrinsic photoluminescence stems from impurities or crystal defects embedded in the material. These impurities and defects which induce photoluminescence are often called activators.

1.3.1 Excitons

When an electron is removed from the valence band due to excitation, it leaves behind a *hole*. This hole can move inside the crystal and has a charge equal to that of the electron but with opposite sign (positive). The hole disappears when the electron returns to its initial energy level. The conduction band electron and the valence band hole interact with each other through the Coulomb force resulting in the formation of an electron-hole pair called an exciton. Excitons can be compared to positronium atoms (electron bound to a positron) and although neutral, they can travel throughout the crystal much like an

atom in free space. The Coulombic interaction between the electron and the hole results in the lowering of the total energy of the exciton relative to the forbidden energy gap. Therefore, these quasi-particles are responsible, upon recombination, for sharp structures within the forbidden band gap in low temperature PL spectra.

There are two types of excitons, the Frenkel and the Wannier-Mott excitons. For Frenkel excitons, the electron and the hole are tightly bound together and they have a radius of the order of the crystal lattice unit cell. They are found mostly in ionic crystals where there is strong electron-hole interaction. However, they have also been observed in wide-gap semiconductors and even in some organic materials. Wannier-Mott excitons, the type observed in the layered transition metal dichalcogenides, are more common in semiconductors. The Coulomb interaction is screened by the valence electrons via the large dielectric constant and causes the electron-hole binding to be weaker than in the Frenkel excitons. Wannier excitons are stable at relatively low temperatures, when the binding energy of the excitons is greater than the thermal energy. The following Schrödinger equation, also know as the Wannier equation, represents an excitonic envelope function describing the relative motion of the electron-hole pair [21]:

$$\Big[-\frac{\hbar^2}{2\mu}\nabla_r^2 - \frac{e^2}{\epsilon r}\Big]\phi(\mathbf{r}) = E_r\phi(\mathbf{r}) \tag{1.3}$$

Where $\frac{1}{\mu} = \frac{1}{m_e} + \frac{1}{m_h}$, μ is the reduced mass of the electron-hole pair with m_e and m_h being the effective masses of the electron and the hole respectively. ϵ is the dielectric constant of the material and r is the relative coordinate of the electron-hole pair. Because the Wannier equation is analogous to the hydrogen case, the energy eigenvalues are obtained as:

$$E_r = -\frac{\mu e^4}{2\hbar^2\epsilon^2}\Big(\frac{1}{n^2}\Big) \equiv -E_B\Big(\frac{1}{n^2}\Big) \tag{1.4}$$

Where $n_B = 1, 2...$ is the principal quantum number and E_B is the exciton Rydberg energy (binding energy) which can also be given by:

$$E_B = \frac{\mu e^4}{2\hbar^2\epsilon^2} = \frac{e^2}{2a_B\epsilon} = \frac{\hbar^2}{2\mu a_B^2}, \tag{1.5}$$

where $a_B = \frac{\epsilon\hbar^2}{\mu e^2}$ is the Bohr radius. The general equation of the total exciton energy is basically the gap energy E_g minus the exciton's binding energy:

$$E_n = E_g - E_B\Big(\frac{1}{n^2}\Big) \tag{1.6}$$

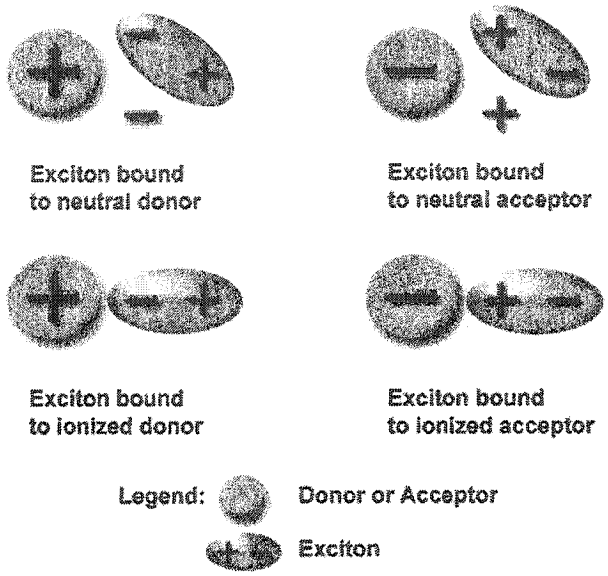

Figure 1.2: Bound exciton complexes formed by impurities or crystal defects.

The exciton can either dissociate into a free electron-hole pair or recombine radiatively to produce a photon after a certain time. Since the Wannier exciton, also called free-exciton, is a mobile quasi-particle able to travel through the crystal, an extra energy term must be added to 1.6:

$$E_n = E_g - E_B \frac{1}{n^2} + \frac{\hbar^2 K_c^2}{2M} \tag{1.7}$$

where $M = m_h + m_e$ is the total mass of the electron-hole pair and K_c is the center of mass wave number. This additional energy term causes the free exciton emission lines to undergo thermal broadening corresponding to an increase in width of the energy distribution.

1.3.2 Bound excitons

It is possible for the excitons to be trapped to an impurity or defect giving rise to a second type of Wannier excitons: Bound excitons. The binding energy of the exciton to the defect or impurity center is quite small, in general in the range of a few meVs. Consequently, it is only at very low temperatures that bound excitons are best observed. Excitons may be bound to neutral donors/acceptors or ionized donors/acceptors forming complexes shown in Figure 1.2. It is possible to identify the nature of the impurity

centers by applying a magnetic field to the sample, inducing a characteristic Zeeman splitting for each type of impurity [22]. The energy of the bound exciton is lower than that of the free-exciton by an amount equal to the binding energy E_I of the exciton to the impurity:

$$E_{bx} = E_g - E_B - E_I \tag{1.8}$$

The concentration of impurities in a material need not be very high to produce intense bound exciton radiative recombination due to the high capture cross section value of the impurity centers. Once the excitons are bound to the center, they can recombine radiatively in a direct optical transition process. The momentum conservation law stated in section 1.2.1 no longer applies to the exciton since the localized state of the electron-hole pair in real space implies, by Fourier transformation, an extension in momentum (k space) [21]. Concordantly, direct photoluminescence of bound excitons can be observed in indirect gap semiconductors. Photoluminescence of bound excitons can be characterized by its very sharp lines at energies below that of the free-exciton lines(if seen). In contrast to the free-exciton, thermal broadening does not occur for the bound exciton because it is localized at the impurity center and has no kinetic energy.

1.3.3 Phonons

As briefly stated in section 1.2.1, a phonon is a quantized vibration of the crystal lattice. The basic relevant theory can be described with a simple model of a linear chain consisting of two alternating types of atoms differing only by their mass. The elementary cell is thus composed of one heavy atom and one light atom. The atoms in this one dimensional system can vibrate in a infinite number of ways. However any atomic motion can be represented by the sum of fundamental vibrations, independent from one another, called normal vibrational modes. Longitudinal optical (LO) and longitudinal acoustical (LA) phonons are created if the atomic displacement occurs in the direction of the linear chain whereas transverse optical (TO) and transverse acoustical (TA) phonons come from a perpendicular motion in reference to that same chain. Vibrational modes are not exclusively related to the host lattice; they can also originate directly from impurity centers and are then called local modes.

In three dimensions, the total number of degrees of freedom (number of normal modes possible) is equal to $3gN$, where g is the number of atoms in the elementary cell and N is the number of cells in the crystal. Thus the degree of freedom in the linear model

extended to a three dimensional lattice is equal to six: two TO, two TA, one LO and one LA. Phonons are mainly responsible for the heat capacity of the crystal and act as the primary mechanism for heat dissipation. Hence, crystal vibrations play a major influence on photoluminescence in solids as they offer an alternate nonradiative recombination mechanism to excited electrons in the form of phonon emission.

1.3.4 Phonon interactions

For bound exciton photoluminescence, a weak to moderate electron-phonon coupling leads to phonon replicas of the principal bound exciton emission lines. Weaker in intensity than the principal lines, these replicas are displaced towards the lower energies of the PL spectrum by an amount of energy equal to that of the emitted phonons. The replicas are well-resolved from one another and from the principal bound exciton lines (also called zero-phonon lines).

The phonon replicas originating from a strong electron-phonon coupling can be described, at very low temperatures, by the simple Poisson function for interaction with a single vibrational mode of energy $\hbar\omega$ [23]:

$$F(h\nu_0 + n\hbar\omega) = \frac{e^{-S}S^n}{n!} \tag{1.9}$$

where $n = 0, 1, 2...$ $h\nu_0$ represents the energy of the initial transitions and S, called the Huang-Rhys factor or multiphonon parameter, describes the mean value of the number n of phonons created and ultimately expresses the strength of the electron-phonon interaction. The intensity of the zero-phonon line is proportional to e^{-S}, therefore the stronger the electron-phonon coupling, the weaker the zero-phonon line. For S$\approx$10 the line becomes virtually invisible and the envelope of the phonon replicas can be essentially represented by a Gaussian [24]. Strong electron-phonon coupling also broadens the phonon replicas due to direct coupling to a greater range of vibrational modes, creating a broad-band shape. However, at very low temperatures, the phonon replicas may still be distinguished before they completely fade out due to thermal broadening. Broad-band luminescence created by multiphonon recombination processes has been observed and documented for deep impurity centers or defects in many semiconductors and is also present in the transition metal dichacogenides layered materials studied in this work.

1.3.5 Thermal quenching of the photoluminescence

Photoluminescence intensity eventually declines as the temperature increases due to nonradiative (phonon emission) transitions entering in competition with photon emission. The luminescence efficiency (η), proportional to the PL intensity, is given by the following ratio:

$$\eta = \frac{\rho_r}{\rho_r + \rho_{nr}} \tag{1.10}$$

where ρ_r is the probability for radiative emission assumed to be independent of temperature and ρ_{nr} ,the nonradiative transition probability, with a temperature dependence described by:

$$\rho_{nr} = \rho_{nr_0} e^{-E_q/kT} \tag{1.11}$$

where ρ_{nr_0} is a temperature independent coefficient and E_q, called the thermal activation or thermal quenching energy, represents the energy needed for excited electrons to decay back to the ground state by nonradiative transitions.

Substituting Eq. 1.11 into Eq. 1.10 leads to the temperature dependence of the photoluminescence intensity shown as:

$$I = [1 + C_q e^{-E_q/kT}]^{-1} \tag{1.12}$$

where $C_q = \tau_r/\tau_{nr0}$ assuming that $\rho_{r,nr0} = 1/\tau_{r,nr0}$. This relation, known as the Mott-Seitz formula can be used to determine the activation energy of any thermal quenching process regardless of its origin.

1.4 Models and configuration coordinate diagram

1.4.1 Time-decay model

In order to describe the temperature dependence of the PL time decay, a kinetic model describing the decay from any thermalized many-level system was taken from [25]. Assuming thermal equilibrium after excitation, the bound excitons are canonically distributed amongst the n-sublevels of the isoelectronic-like impurity center T_1. Therefore the total exciton concentration of the center (N^x_{T1}) is given as:

$$N_{T1}^{x} = \sum_{i=1}^{N} N_i^x \tag{1.13}$$

and the relationship between the sublevels can be described with:

$$N_i^x/g_i = (N_j^x/g_j) \cdot exp(\Delta_{ji}/kT) \tag{1.14}$$

where g_i and g_j are the degeneracies of the i-th and j-th levels respectively and Δ_{ji} is the energy between the j-th and the i-th level. From these assumptions, the experimentally observed decay time may be expressed as:

$$\tau_{Rx} = \frac{\sum_{i=1}^{N}(g_i/g_l) \cdot exp(\Delta_{il}/kT)}{\sum_{i=1}^{N}[\tau_{Ri}^{-1} + \tau_{th}^{-1}] \cdot (g_i/g_l) \cdot exp(\Delta_{il}/kT)} \tag{1.15}$$

where Δ_{il} is the energy between the i-th level and the lowest excited level $i = 1$ ($\delta_{11} = 0$) and τ_{th} is the decay time for any thermally activated process removing population from the levels. It is assumed [25] that this thermal quenching is due to a single thermally activated process given by:

$$\tau_{th}^{-1} = \tau_0^{-1} \cdot exp(-E_a/kT) \tag{1.16}$$

where E_a is the activation energy of the quenching and τ_0^{-1} is of the order of the vibrational lattice frequency $10^{12} - 10^{13} s^{-1}$ and is assumed to be independent of temperature.

1.4.2 Kinetic recombination model

The temperature dependence of the integrated PL intensity was also studied and measured for three of the MoS_2,WS_2 and WSe_2 synthetic samples. The experimental results were then analyzed using a similar kinetic recombination model proposed for the n-type isoelectronically nitrogen-doped GaP [26]. The equations of the original model were slightly modified to take into account two distinct radiative channels instead of one: a channel for bound exciton recombinations from an impurity center (T_1) and a second one for deep level recombinations from a crystal defect center (T_2) which acts as a shunt path to the excitonic PL intensity. Under the assumption of low-level excitation, thermal equilibrium and including the modifications just mentioned, the equations which describe the kinetic behavior of the minority carriers (p) in an n-type material are given as:

$$\dot{p} = G - p \cdot \nu_{th} \cdot \sigma_{px} \cdot (N^e_{T1} - N^x_{T1}) + \frac{N^x_{T1}}{\tau_{xp}} - p \cdot \frac{N^e_{T2}}{N_{T2}} \cdot \left(\frac{1}{\tau_{Rbb}} + \frac{1}{\tau_{Nbb}}\right), \tag{1.17}$$

$$\dot{N}^x_{T1} = p \cdot \nu_{th} \cdot \sigma_{px} \cdot (N^e_{T1} - N^x_{T1}) - N^x_{T1} \cdot \left(\frac{1}{\tau_{Rx}} + \frac{1}{\tau_{Nx}} + \frac{1}{\tau_{xp}}\right) \tag{1.18}$$

Here p is the concentration of the holes, N_{T1} and N_{T2} are the total concentration of impurity and deep centers, N^e_{T1} and N^e_{T2} are the concentration of electron-occupied T_1-impurity and $T2$-deep centers, N^x_{T1} is the concentration of centers which have an exciton bound to the site, $\tau_{Rx}(\tau_{Nx})$ is the bound exciton radiative (nonradiative) recombination time, $\tau_{Rbb}(\tau_{Nbb})$ is the T_2 deep level radiative (nonradiative) time (hole shunt-path capture time), σ_{px} is the hole capture cross section by electron occupied centers, ν_{th} is the thermal velocity of minority carriers, τ_{xp} is the T_1 center exciton hole thermalization time and G is the excitation rate.

This model considers that under steady state conditions the electron-occupied impurity and deep center concentrations are in thermal equilibrium with the majority carrier concentrations:

$$N^e_{T1} = f_{e1} \cdot N_{T1}, N^e_{T2} = f_{e2} \cdot N_{T2} \tag{1.19}$$

where f_{e1} and f_{e2} are the electron occupancy probabilities of T_1 and T_2 centers respectively. The model also assumes a low-level excitation $p \ll N_{T2}, N^e_{T1} \gg N^x_{T1}$ and that all deep T_2 centers are electron-occupied ($f_{e2} = 1$,$N^e_{T2} = N_{T2}$) in the considered temperature range. For these assumptions, the steady-state solution ($\dot{N}^x_T, \dot{p} = 0$) of Eqs. 1.17 and 1.18 yield the following relationship for the quantum efficiencies of the excitonic radiative recombination $\eta_{Rx}(T)$ and the broad-band emission $\eta_{Rbb}(T)$:

$$\eta_{Rx} = \frac{N^x_{T1}}{\tau_{Rx}} \cdot \frac{1}{G} = \left(1 + \frac{\tau_{Rx}}{\tau_{Nx}}\right)^{-1} \cdot \left[1 + \frac{\tau_{cp}}{\tau_{Rbb}} \cdot \left(1 + \frac{\tau_{Rbb}}{\tau_{Nbb}}\right) \cdot \left(1 + \frac{\tau_{Rx}}{\tau_{xp}}\right)\right]^{-1} \tag{1.20}$$

$$\eta_{Rbb} = \frac{p}{\tau_{Rbb}} \cdot \frac{1}{G} = \left(1 + \frac{\tau_{Rbb}}{\tau_{Nbb}}\right)^{-1} \cdot \left[1 - \left[1 + \frac{\tau_{cp}}{\tau_{Rbb}} \cdot \left(1 + \frac{\tau_{Rbb}}{\tau_{Nbb}}\right) \cdot \left(1 + \frac{\tau_{Rx}}{\tau_{xp}}\right)\right]^{-1}\right] \tag{1.21}$$

where

$$\tau_{cp} \equiv (\nu_{th} \cdot \sigma_{px} \cdot N^e_{T1})^{-1} \tag{1.22}$$

is defined as the capture time of holes by electron-occupied centers. The temperature behavior of the radiative recombination intensity of the excitonic and broad-band regions can therefore be described as a function of the lifetimes $\tau_{Rx}(T), \tau_{cp}(T), \tau_{xp}(T), \tau_{Nx}, \tau_{Rbb}$, and τ_{Nbb}.

$\tau_{Rx}(T)$, the bound exciton radiative recombination time defined by Eq. 1.15 without the thermally activated process term (i.e $E_a \rightarrow \infty, \tau_{th}^{-1} = 0$) can be rewritten as:

$$\tau_{Rx}(T) = \frac{\sum_{i=1}^{N}(g_i/g_l) \cdot exp(\Delta_{il}/kT)}{\sum_{i=1}^{N} \tau_{Ri}^{-1} \cdot exp(\Delta_{il}/kT)} \tag{1.23}$$

$\tau_{cp}(T)$, defined previously as the hole capture time, depends on ν_{th}, σ_{px} and the concentration of the electron-occupied radiative centers N_{T1}^{e} (which are in thermal equilibrium with the majority-carrier concentration n_0). The temperature dependence of N_{T1}^{e} may be extracted from the low-level excitation and non-degenerate occupation probability f_{T1}^{e} equation given by [27]:

$$f_{T1}^{e} = N_{T1}^{e}/N_{T1} = [1 + g_T \cdot \frac{N_C}{n_0} \cdot exp(-E_{T1}/kT)]^{-1} \tag{1.24}$$

where $g_T = 1$ is the level of degeneracy, E_{T1} is the binding energy of the electron to the impurity center and N_C is the density of states of the conduction band, with an electron effective mass m_e, given by the well-known equation:

$$N_C = 2 \cdot (2\pi \cdot m_e \cdot kT/h^2)^{3/2} \tag{1.25}$$

Inserting Eq. 1.25 into 1.24 and isolating N_{T1}^{e}, setting $\nu_{th} = (3 \cdot kT/m_h)^{1/2}$ (m_h hole effective mass) and attributing a certain value to σ_{px} (see section 3.5.2) will finally yield the hole capture time $\tau_{cp}(T)$.

τ_{xp}, the time of the excitonic-hole thermalization can be written as [28]:

$$\tau_{xp} = 2 \cdot exp(E_h/kT) \cdot \left(\sigma_{px} \cdot \nu_{th} \cdot N_V\right)^{-1} \tag{1.26}$$

where 2 is the spin degeneracy factor, E_h the hole binding energy and N_V is the density of states in the valence band defined similarly as N_C (Eq. 1.25) save for the electron effective mass m_e is replaced by the hole effective mass m_h.

Much like σ_{px}, the last three parameters τ_{Nx}, τ_{Rbb}, and τ_{Nbb} will be assigned certain values based on data acquired from previous and current experiments. Details regarding the application of the kinetic recombination model to the experimental data are discussed in section 3.5.2.

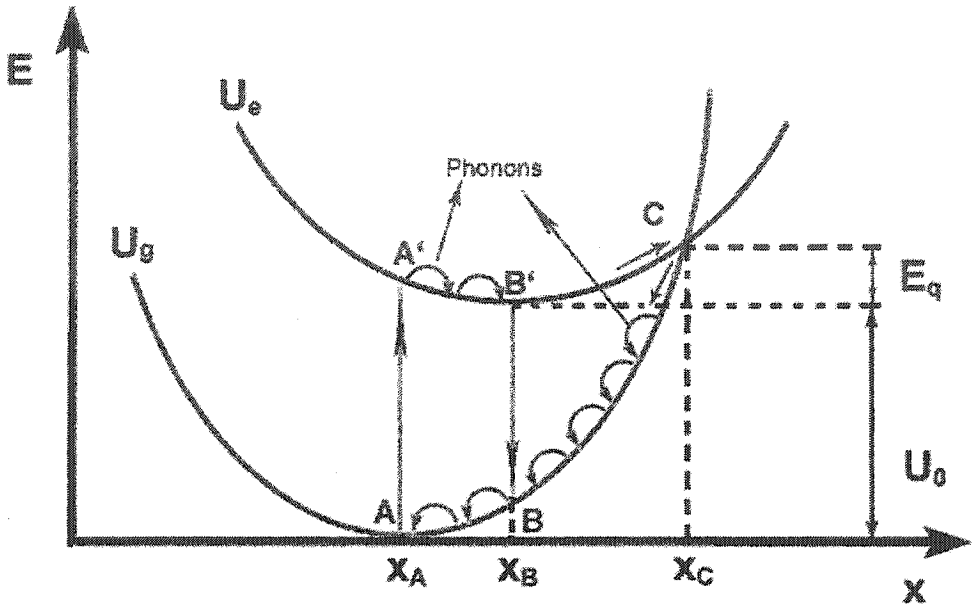

Figure 1.3: Configuration coordinate diagram depicting an absorption process A→A', a radiative transition B'→ B and a nonradiative transition via the C point.

1.4.3 Configuration coordinate diagram

The configuration coordinate (CC) model effectively describes, within the adiabatic approximation, the interactions between electronic and vibronic (lattice vibration) transitions. This model, essentially a simplified version of the multiphonon optical transition theory derived by Huang and Rhys [29], employs a single configuration coordinate (x) representing one aspect of the geometrical configuration of the active center with its nearest lattice atom neighbors. Although this one-dimensional assessment can only lead to approximate results, the CC model nevertheless provides valuable information on radiative and nonradiative recombination processes in the form of a configuration coordinate diagram schematically illustrated in Figure 1.3.

The absorption and emission processes in the CC diagram follow the Frank-Condon principle which states that the time for a transition between two electronic energy levels is much shorter than the vibrational period of nuclei. The nuclei are therefore regarded as stationary and the optical transitions in Figure 1.3 are depicted as vertical lines. At low temperatures, electrons raised from the ground to the excited state via the A → A'

absorption transition are of higher energy than the minimum configurational position of the excited state x_B. Since the lifetime of the excited state is long compared to the lattice vibrational period, the electrons first relax to the state minimum by phonon emissions. Thereafter, the excited electrons may recombine radiatively by the B' $\rightarrow$ B transition and relax to the ground state equilibrium position (x_A) once more by emitting phonons. These relaxation periods producing phonons cause the emitted photons to always be of lower (higher) energy (wavelength) than the initially absorbed photon, an experimentally well-known process called Stoke's law. As the temperature increases, the configurational position x_B of the active center can increase to x_C where both ground and excited states intersect at point C. The connection between the two curves now allows excited electrons to reach the ground state by nonradiative transitions, exclusively emitting phonons. It should be noted that the absorption process shown by the A $\rightarrow$ A' transition must raise the electron to an energy level below that of the C point, otherwise a nonradiative transition to the ground state could occur even at low temperatures.

In order to construct the CC diagram, one must represent the potential energy curves of the ground and excited states, corresponding to U_g and U_e, by the following mathematical equations

$$U_g = \frac{1}{2}k_g(x - x_A)^2 \tag{1.27}$$

$$U_e = \frac{1}{2}k_e(x - x_B)^2 + U_0 \tag{1.28}$$

$$k_{(g,e)} = M\omega_{(g,e)}^2 \tag{1.29}$$

Where M is the mass of the active center, ω_g and ω_e are the vibrational frequency of the ground and excited states respectively, U_0 refers to the energy difference between the two states and x describes the distance between the luminescent center and its closest atomic neighbor within the crystal lattice. Four parameters are now required to sketch the potential energy curves of the CC diagram: k_g, k_e, U_0 and x_B (x_A is taken as the origin, thus is equal to 0). Phonons and other energy values from the experimental PL spectra at different temperatures can be extracted to calculate the missing parameters using a series of formulas in the frame of the semiclassical approximation given in [30].

The CC diagram is not limited to a single pair of curves. Consequently, several luminescent centers may be represented on one diagram. The configuration coordinate x is linked to the electron-phonon interaction strength. The stronger the electron-phonon

coupling, the greater the separation between the ground and excited state in x. Luminescent center with weak electron-phonon interaction such as bound exciton complexes may therefore be represented in the CC diagram with a zero offset curve relative to the ground state.

1.5 Photoconductivity effects

Photoconductivity (PC) can be defined as the change in resistance due to the generation of extra carriers in a material following absorption of light. It is a combination of optical excitation and transport phenomena. Although generally complex, PC offers a means of studying many physical properties of the material of interest, which in this case is the energetic position of the impurity levels in synthetic single crystals. PC is a well-known and extensively researched process but since it is not the main topic of research in this work, this section will not dwell on detailed descriptions of the many PC mechanisms but rather be limited to a brief explanation of the PC process of interest: impurity PC.

Analogous to photoluminescence, there can be two types of photoconductivity, intrinsic and extrinsic. Intrinsic PC refers to the study of host lattice related conductivity effects while extrinsic PC studies the effects due to impurities. Although electrically neutral, excitons bound to impurities produce peaks in photoconductivity spectra [31]. The change in conductivity due to bound excitons can be achieved through several processes. A free carrier can be thermally excited from an exciton-ionized impurity complex, leaving behind a neutral impurity. A bound exciton may hop off into the free-exciton state and then dissociate into free carriers. Finally, an exciton can also be annihilated near a neutral impurity simultaneously exciting an electron to the conduction band, a process called Auger effect.

Since it is possible to detect bound excitons in materials such as transition metal dichalcogenides, impurity photoconductivity may be thus used to complement photoluminescence measurements.

Chapter 2

Experiment

This chapter will treat the experimental part of this research. First the single crystal and powder samples will be presented in 2.1. Section 2.2 contains a detailed description of the two types of experimental setups used throughout this work and a short summary of the steady-state PL, time-resolved and PL intensity dependence measurements performed on the samples. A brief review on the PC measurements undertaken will be presented in section 2.3. The last section of this chapter will deal with the experimental techniques utilized for the intercalation of different halogen molecules in the natural MoS_2 single crystals.

2.1 Samples

Several samples of the layered transition metal dichalcogenides 2H-MoS_2, 2H-WS_2 and 2H-WSe_2 have been investigated in this work. The research focused mainly on the synthetic single crystals grown by vapor transport method; however, naturally occurring MoS_2 single crystals as well as several commercial MoS_2 and WS_2 powders were also examined. A list of all the samples is shown in Table 2.1. Each sample will now be referred to their appointed names given in the table.

2.1.1 Single crystals

The n-type 2H-WS_2 and 2H-WSe_2 crystals were provided by Dr. Kulyuk from the Institute of Applied Physics, Academy of Science in Moldova where iodine and bromine were used as transport gas during the fabrication of these crystals [32]. The synthetic n-type 2H-MoS_2 samples produced with chlorine were supplied by Dr. Francis Lévy at

Single crystals			
Name	Compound	Origin/Batch #	Transport gas
Sample 1	2H-MoS_2 Synthetic	Montreal 565	chlorine
Sample 2	2H-MoS_2 Synthetic	Lausanne 200787	chlorine
Sample 3	2H-MoS_2 Synthetic	Lausanne 10887	chlorine
Sample 4	2H-MoS_2 Natural	Gatineau Park N/A	N/A
Sample 5	2H-WS_2 Synthetic	Moldova ER15	bromine
Sample 6	2H-WS_2 Synthetic	Moldova ER9	iodine
Sample 7	2H-WSe_2 Synthetic	Moldova ER17	iodine
Powders			
Name	Compound	Manufacturer	Purity
Powder 1	2H-MoS_2 Natural	Aldrich #234842	99%, size$< 2\mu$m
Powder 2	2H-MoS_2 Natural	Riedel-de Haën #13312	99.5%, size $< 2\mu$m
Powder 3	2H-MoS_2 Natural	Fluka #69860	95%, size$\sim 2\mu$m (max. $40\mu m$)
Powder 4	2H-WS_2 Synthetic	Aldrich #24363 – 9	99%, size$< 2\mu$m

Table 2.1: List of samples

the applied physics laboratory, École Polytechnique Fédérale in Lausanne, Switzerland and by Dr. Leonelli from the department of physics at the University of Montréal.

Natural n-type 2H-MoS_2 single crystals were taken from a molybdenite mine in Gatineau Park, Québec, Canada. Fortin et. al. [33] demonstrated that the energetic positions of the intrinsic spectral structures were the same in both synthetic and natural MoS_2. The roughness of the natural MoS_2 single crystals surfaces is the only physical difference distinguishing the natural samples from the synthetic ones.

Due to the weak interacting van der Waals forces existing between the layers of the single crystals, the samples were easily cleaved to obtain smooth and clean surfaces. Therefore no chemical etching or mechanical polishing was required. The thickness of each crystals were of the order of a few tens of micrometers with diameters varying from 1 to 3 mm. The MoS_2 and WS_2 crystals had respectively bright blueish and greenish reflective metal looks to them.

2.1.2 Powders

Three different kinds of commercial MoS_2 powders were purchased. The first MoS_2 powder was manufactured by Aldrich, the second by Riedel-deHaën and finally the third by Fluka. All three powders were produced from natural molybdenite and underwent chemical heat treatments involving chlorine for cleaning and purifying purposes. A WS_2 powder was also purchased from Aldrich however this material was synthetic in nature. Since there exists two stacking polytypes for these materials (Hexagonal (2H) and Rhombohedral (3R)) all four powders underwent powder x-ray diffraction using the facilities at the University of Ottawa to confirm that they had the same hexagonal structure as the single crystals.

Thin circular pellets were fabricated from the powders in order to take PL. A simple but effective apparatus consisting of a piston and a hollow cylinder was used to compress the powders into the pellets with the aide of a mechanical press. Pressures in the range of $\sim 5 \times 10^6$ Pascals were applied to compress the materials into reasonably structurally stable pellets. Typical thickness of the samples using $\sim$ 0.300 gram of powder ranged between 0.5 mm and 1.5 mm. Samples with a thickness lower than 0.5 mm were extremely fragile and could not be used for PC or PL. The MoS_2 and WS_2 pellets were quite fragile and had to be handled with care. While the MoS_2 powders compressed easily into pellets, the WS_2 pellets were harder to make since the powder stuck to the walls of the compression apparatus.

Measurements	Setup 1(Ottawa)	Setup 2(NRC)	Setup 3(Konstanz)
Steady-state PL	Fig. 3.2 sample 5	Fig. 3.3 sample 1	Fig. 3.1
(PL spectra or	Fig. 3.5	Fig. 3.4	Fig. 3.2 sample 1,7
Integral PL	Fig. 3.8 sample 5	Fig. 3.7	Fig. 3.3 sample 5
Intensity)	Fig. 3.11		Fig. 3.6
	Fig. 3.14 sample 5		Fig. 3.8 sample 1,7
	Fig. 3.19		Fig. 3.14 sample 1,7
	Fig. 3.21		
Intensity dependence PL	Fig. 3.16	Fig. 3.17	
		Fig. 3.18	
		Fig. 3.20	
Time-resolved PL	Fig.3.9		

Table 2.2: Results obtained from each experimental setups

2.2 PL measurements

Several types of PL measurements such as steady-state PL, intensity dependent PL and time-resolved PL measurements were performed with various experimental setups from the University of Ottawa, the University of Konstanz in Germany and from the National Research Council (NRC) in Ottawa. The following subsections will present detailed layouts of some of these experimental setups as well as well as describe the three types of measurements performed on the samples. In order to reduce confusion, Table 2.2 was constructed to inform which setups were used for every result presented in chapter 3.

2.2.1 Experimental setup 1

The experimental setup located at the University of Ottawa is shown in Figure 2.1 and presents three separate geometries (I), (II) and (III). While (I) and (II) offer two different sample excitation geometries utilized for steady-state and intensity dependence PL measurements(see inset), the third geometry (III) is employed for PL time-resolved measurements.

In all cases several samples were fixed to a copper holder with teflon tape (shown in Figure 2.2) and then placed in a Janis research model 8CNDT liquid helium cryostat with optical access through four windows, each consisting of two vacuum spaced fused quartz plates. The cryostat permitted PL measurements at temperatures as low as 2K.

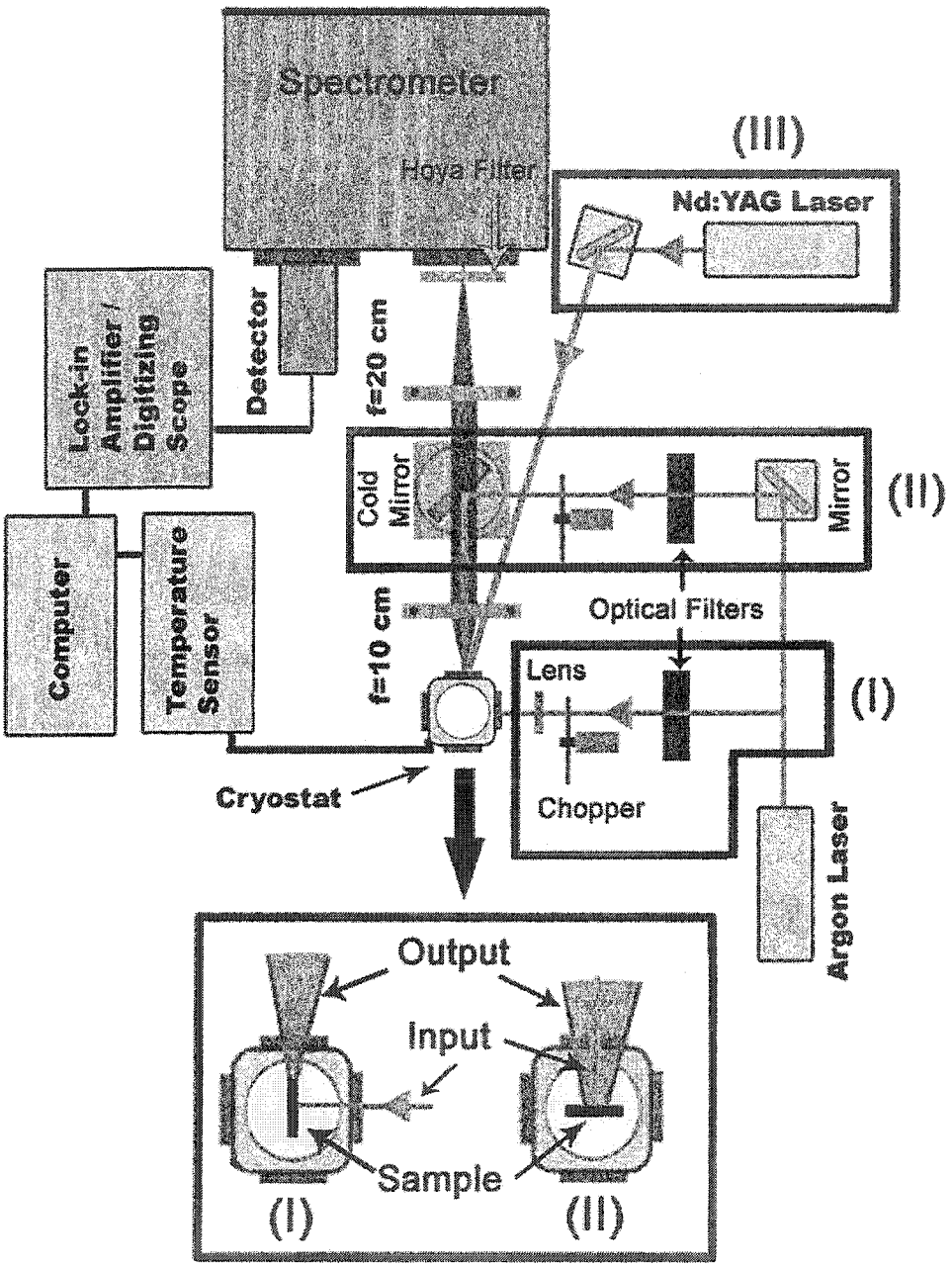

Figure 2.1: PL experimental layout at the University of Ottawa. Three different PL geometries (I,II and III) are shown. The inset illustrates the input(laser) and output(PL) for (I) and (II).

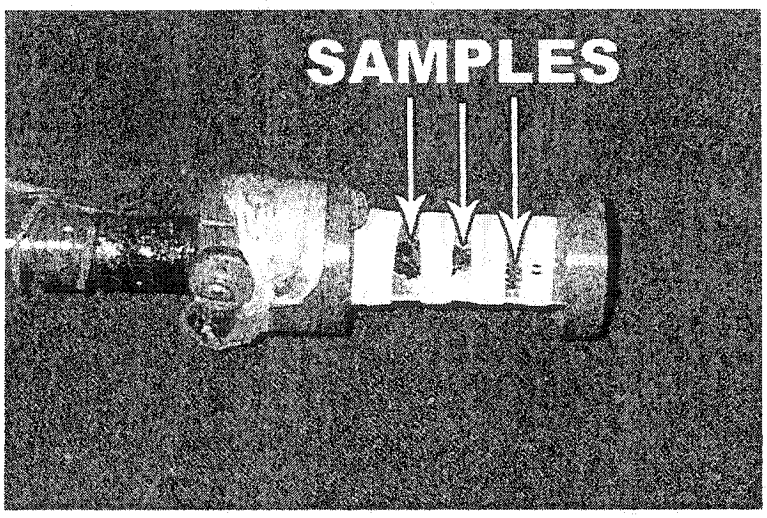

Figure 2.2: PL copper holder with teflon strips

The cooling system of the Janis cryostat is comprised of a computer-controlled valve for the pumping port, a manual needle valve to control the flow on liquid helium inside the sample chamber and a heater placed beneath the sample to regulate the amount of liquid helium (or gas) within the sample chamber. Specific temperatures are reached and maintained by varying the settings on all three components just mentioned. Two calibrated silicon diode sensors provide the temperature readings. One sensor is placed just above the sample in a copper cylinder while the second is placed at the bottom of the sample chamber. Superfluid helium temperatures ($T \approx 1.8 - 2\text{K}$) could be attained by evaporative cooling: pumping the "hot" helium gas from the sample chamber therefore lowering the temperature even further. At 2K, the samples are completely submerged in superfluid liquid helium while at higher temperatures the samples are surrounded by a cold helium gas.

The light output from the sample was picked up by a lens at a distance equal to its focal length (10 cm). The quantity of light which could be collected by the lens was limited by the optical window of the cryostat. A second lens with a focal length of 20 cm then focused the light into a 1 meter McPherson Instrument model 2061 spectrometer. The optical arrangement was assembled to match as best as possible the numerical aperture of the spectrometer thus optimizing the PL signal. The spectrometer used a holographic diffraction grating of 300 grooves/mm. The grating allowed a sweeping range of 6.7 eV (185 nm) to 0.5 eV (2480 nm). The spectral resolution of the signal could be altered by adjusting the spectrometer's input and output slits. At 2 mm, the maximal

aperture size of the slits, the resolution was approximately 10 meV. A high pass optical filter (Hoya IR-80) was placed in front of the spectrometer's entrance to block out stray light from various reflections on the experimental arrangement. This filter eliminated any wavelength above (below) 1.59 eV (780 nm) and transmited at over 90% below (above) 1.51 eV (820 nm). The PL signal entering the spectrometer was finally collected by a detector, sent to the lock-in amplifier or digitizing scope and then transferred to the computer. Two different detectors were used for the WS_2 and MoS_2 samples. An S−1 photomultiplier tube (PMT) operating with a high-voltage source was used to detect the WS_2 PL signal while a nitrogen-cooled germanium detector was used for the MoS_2 samples since its PL signal was beyond the sensitivity of the PMT.

For the (II) geometry a long wavepass filter (cold mirror) was placed between the two lenses. The cold mirror reflected the excitation light at normal incidence on the sample but transmitted the infrared luminescence emanating from the sample to the spectrometer. It also acted as a shield by filtering out parasitic light produced by the laser light reflections on the optical windows of the cryostat.

2.2.2 Experimental setup 2

Figure 2.3 represents the experimental arrangement used at the NRC. The samples were mounted on a copper holder in a similar fashion as for experimental setup 1. The helium gas bath cryostat permitted measurements at temperatures from 4.2K and up. The cooling system's automated temperature control with feedback signal achieved very stable temperatures up to 180K and did not require constant attention compared to the manual temperature control of experimental setup 1.

A set of mirrors was first used to redirect the excitation light into a lens, focusing the beam on the sample at normal incidence. A short wave pass filter was placed before the lens to eliminate any wavelengths lower (higher) than 1.65 eV (750 nm) produced from the excitation source. The output luminescence from the sample was redirected by another set of mirrors to a detector. Similarly to experimental setup 1, a long wave pass filter of 1.91 eV (650 nm) (cold mirror) was used to reflect the laser light to the sample while transmitting the emitted radiation from the sample to the detector. Two more long wave pass filters were placed at the opening and inside the detector to remove any stray light with wavelengths higher (lower) than 1.73 eV (715 nm).

A Fourier transform infrared (FTIR) system coupled to a InGaAs model MB-160 solid-state detector with a maximum resolution of 1 meV was used collect the PL of the

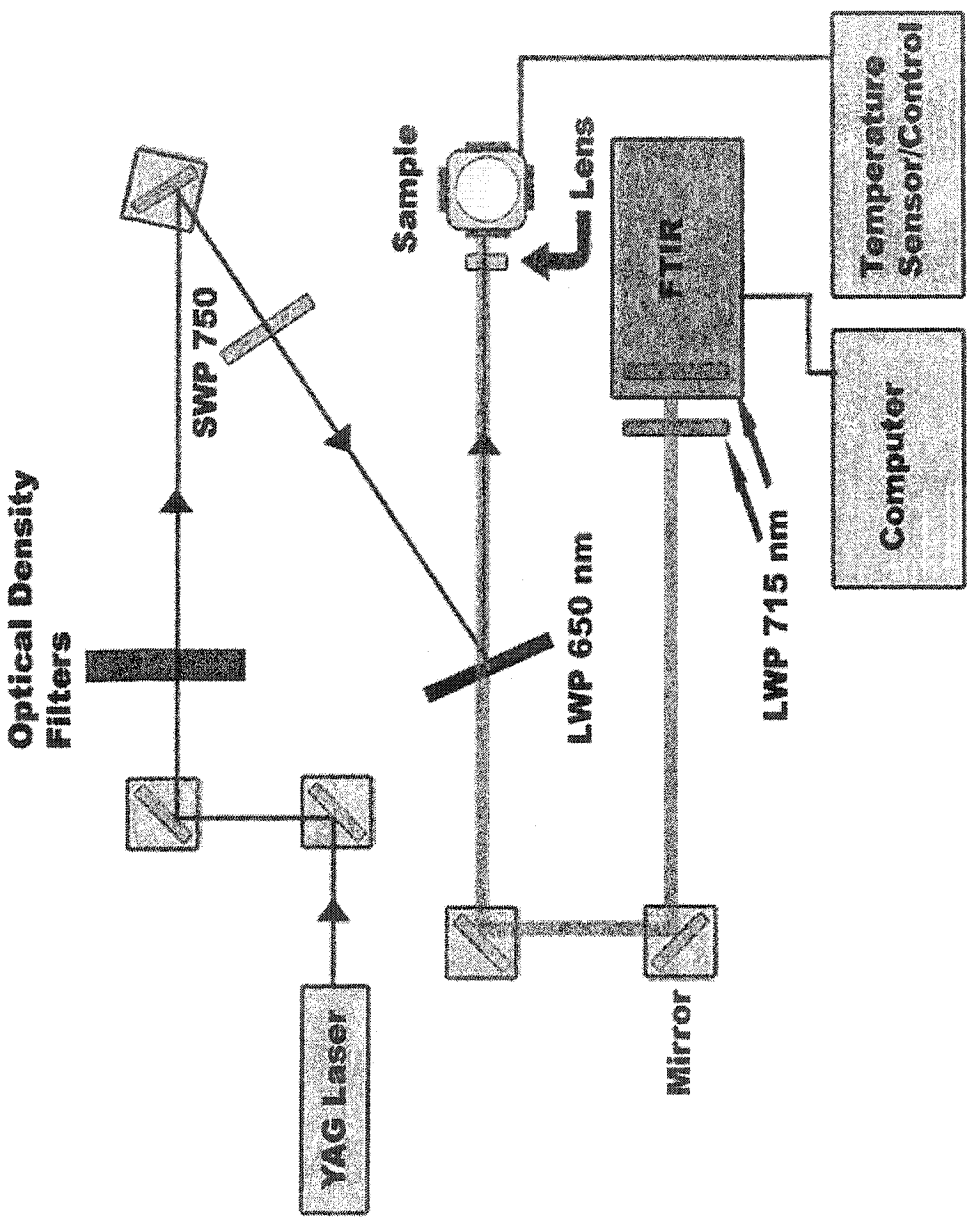

Figure 2.3: PL experimental layout at the National Research Council.

MoS_2 samples. An FTIR detector is essentially a Michelson interferometer measuring the intensity of light as a function of time. The computer then applies the Fourier transform to obtain the intensity as a function of wavelength. The PL spectra becomes progressively more detailed with increasing time. Being able to observe the full spectral region quasi-instantaneously permits fast modifications of the setup and computer settings, offering a serious advantage especially if the luminescence spectral region is unknown.

2.2.3 Steady-state measurements

Steady-state measurements were performed in both (I) and (II) geometries of experimental setup 1 using a standard lock-in detection technique. The excitation source consisting of an argon laser in multiline mode (from 488 to 514 nm) was chopped and redirected by a set of mirrors through a lens, hitting the sample at normal incidence. The luminescence was then collected as described in section 2.2.2. PL steady-state measurements were also acquired at the University of Konstanz using a lock-in detection technique with a similar experimental layout as the one in Ottawa. The excitation light was provided by a diode-pumped cw solid-state laser (532 nm) as opposed to a continuous multiline argon laser. The Konstanz layout will now be referred to as experimental setup 3. The spectra taken from both arrangements were corrected for the wavelength-dependent response of the optical systems. Finally, PL spectra were obtained from the experimental setup 2 where a frequency-doubled cw diode pumped YAG laser (532 nm) provided the excitation.

Although PL spectra of the synthetic MoS_2 single crystals were taken at all three locations, the ones taken from experimental setup 2 were superior in resolution and therefore were chosen to illustrate the temperature evolution of the compound in Figures 3.4 and 3.7. Nevertheless, the MoS_2 PL spectra taken with experimental setup 3 were still used for the integral PL intensity measurements presented in Figures 3.8 and 3.14 since they offered more data points in the regions of interest as opposed to the PL spectra from the NRC. The synthetic MoS_2 2K PL spectrum from Konstanz was also displayed in Figures 3.1 and 3.2 as the NRC cryostat could not take any PL measurements below 4.2K. The experimental setup 3 was also used to take the PL spectra of the synthetic WSe_2 single crystals as well as all three characteristic PL spectra in Figure 3.1.

Experimental setup 1 was used to collect PL spectra of the MoS_2 and WS_2 commercial powders, chlorine-treated and untreated natural MoS_2 single crystals and most of the PL spectra on the synthetic WS_2 single crystals samples. Refer to Table 2.2 for the complete list of figures taken by all three experimental layouts.

2.2.4 PL time-resolved measurements

Time-resolved measurements of the WS_2 single crystal presented in section 3.3 were realized with experimental setup 1 using the (III) geometry and enabled us to study the kinetics of the radiative recombination processes. The luminescence decay was investigated under pulsed excitation provided by a frequency doubled Q-switched Nd:YAG laser (532 nm) with a pulse width of $\sim 10^{-8}$s at 10 Hz frequency. The sample was excited at near-normal incidence by the laser without being first focused by a lens. The time decay signal of the PL was detected with the S−1 PMT coupled to a Tektronix 2GS digitizing scope. With this oscilloscope we could register the time evolution of the radiative recombination processes and transferred the data directly to the computer.

2.2.5 PL intensity measurements

Steady-state measurements were performed as a function of excitation intensity with experimental setups 1 and 2. Neutral density filters were placed in front of the excitation source to modify the laser intensity (see Figures 2.1 and 2.3). In both arrangements, a lens focused the laser beam on the samples to a spot size of approximately 800 microns. The maximum power setting of the laser for setups 1 and 2 were approximately 20 mW and 80 mW respectively. Measurements with experimental setup 1 were carried out uniquely in superfluid helium (2K) while intensity measurements with experimental setup 2 were performed at various temperatures between 4.2K and 70K.

2.3 PC measurements

Photoconductive measurements were carried out on the MoS_2 sample 1 and WS_2 sample 5 using two different electrode configurations (A and B) shown in Figure 2.4. The electrodes were formed by evaporating gold and/or indium on the samples.

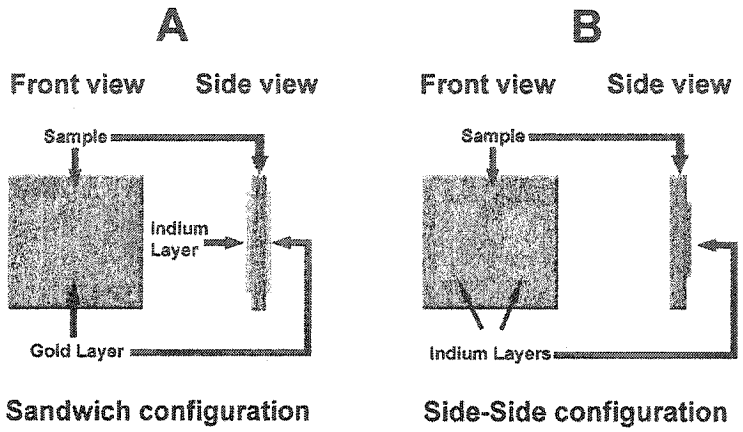

Figure 2.4: Electrode configurations for the PC measurements.

Figure 2.5 illustrates the PC experimental setup used. The light from an intense quartz-iodine lamp was passed through a chopper and focused into the spectrometer using a concave mirror with focal length of 1 m. The wavelength exiting the monochromator was collected and focused on the sample with the same lens configuration as the experimental setup 1. The PC signal was then measured from the voltage drop across a load resistor in series with the sample using a lock-in amplifier and finally sent to the computer were it was plotted as a function wavelength.

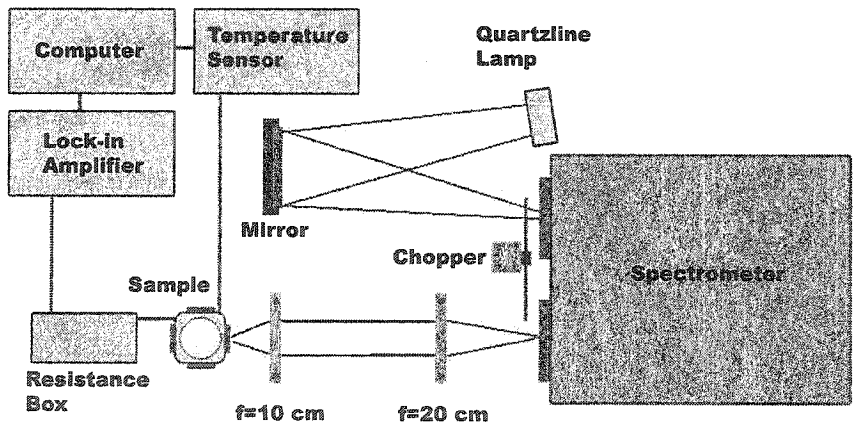

Figure 2.5: PC experimental setup at the University of Ottawa.

2.4 Intercalation of single crystals and powders

Intercalation of halogen molecules in natural MoS_2 single crystals was first attempted shortly after photoluminescence was observed in the synthetic MoS_2 samples. Iodine, bromine and chlorine were used during the intercalation experiments. Pieces of sample 4 were sealed in quartz or thick-walled pyrex tubes with various amounts of iodine, bromine or chlorine. Three different techniques were devised to seal iodine, bromine and chlorine into the tubes. While iodine's and bromine's respective solid and liquid phase at room temperature made the sealing of the tubes relatively simple (the step-by-step procedure is given in Table 2.4), the gaseous state of chlorine required a more complex sealing method. A special setup necessary to seal the chlorine gas, illustrated in Figure 2.6, was therefore constructed under a fume hood. The procedure is described in detail in Table 2.4.

1	Cleave pieces of sample 4 and thoroughly clean the quartz tube with ethanol and distilled water.
2	Insert the samples in the tube.
3	Create a constriction near the end of the tube.
4	For iodine: Insert a few grams of iodine crystals in the tube. For bromine: Place the end of the tube in liquid nitrogen. Add a few drops of bromine in the tube. (Must be done under a fume hut). The bromine should freeze, the following steps should always be done with the tube partly submerge in liquid nitrogen to prevent the bromine from evaporating.
5	Establish a vacuum inside the tube of approximately 10^{-4} Torr, then seal the quartz tube at the constriction.

Table 2.3: Bromine and iodine tube sealing technique.

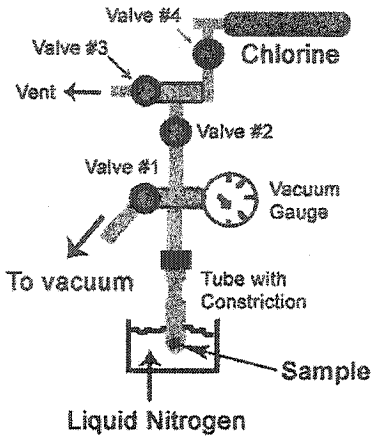

Figure 2.6: Setup used to seal chlorine gas into a tube for the intercalation experiment.

1	From Figure 2.6, Valves (1), (3) and (4) are closed.
2	Follow the first same three steps as the bromine and iodine process
3	Open (1) and establish a vacuum of $\sim 10^{-4}$ Torr. Insert a neutral gas (usually nitrogen) into the system through (3). Close (3) and reopen (1)
4	Repeat step 3 three to four times to thoroughly flush the system.
5	Close (2) then open (4), then again gently open (2) until vacuum gauge indicate atmospheric pressure. Close (2) and (4)
6	Submerge the tip of the tube into liquid nitrogen. The pressure should diminish as the chlorine gas transforms into a liquid and accumulates at the bottom of the tube.
7	When the pressure has stop decreasing, seal the tube.
8	Open (3) and purge the system with nitrogen gas.

Table 2.4: Chlorine tube sealing technique.

Figure 2.7: Quartz tube with natural MoS_2 single crystals and iodine

After the tubes were sealed, they were heated at temperatures ranging from 200 to 800 degrees Celsius in a Lindberg furnace with a temperature control console and left inside the furnace for time periods as short as 24 hours and as long as 1 month. Quartz was used for higher temperatures given its higher melting point and capacity to withstand higher pressures than pyrex. For iodine and bromine, a temperature gradient was applied just before removing the tube from the furnace. This separated the halogens from the samples as the halogen gas solidified or liquified at the lower-temperature end of the tube. Figure 2.7 shows a tube with the MoS_2 natural crystals on one side, and the solidified Iodine on the other.

Chapter 3

Results and discussion

The experimental results as well as their analysis will be presented in this final chapter. While the main focus of this work remains on the MoS_2 material, several measurements have also been performed on the WS_2 and WSe_2 layered compounds to complement the research. The results displayed in this chapter were obtained with various experimental arrangements as discussed in section 2.2.

The first section will introduce the characteristic PL spectra observed in the single crystals. Section 3.2 will describe the temperature dependence of the PL while section 3.3 will deal with the time-resolved measurements. A detailed explanation on the origin of the PL will then be presented in section 3.4. The time-decay and kinetic recombination models introduced in chapter 1 will be applied to the experimental data and a configuration coordinate diagram will be constructed for the MoS_2 compound in section 3.5. Section 3.6 will present the PL intensity dependence of the materials. Finally the last section will present PL measurements on the MoS_2 and WS_2 commercial powders and describe the technique devised to intercalate halogen molecules into natural MoS_2 single crystals.

3.1 Characteristic PL spectra of the synthetic and natural single crystals

Figure 3.1 illustrates the characteristic PL spectra of MoS_2 sample 1 , WS_2 sample 5 and WSe_2 sample 7. Two distinct regions are observed: a high energy excitonic section consisting of several sharp lines and a broad spectral band. The excitonic parts of the synthetic MoS_2 single crystal centered at $E_{ex} = 1.174$ eV and WS_2 centered at $E_{ex} = 1.325$ eV are located approximately 0.1 eV below their respective indirect band gaps (E_g^{ind}) of 1.29 eV [34] and 1.45 eV [35]. Their broad spectral band, with half-widths $\Delta_{bb} \approx 0.1 - 0.12$ eV, are centered at $E_{bb} = 0.95$ eV and 0.97 eV. As for the WSe_2 sample 7, its excitonic region ($E_{ex} = 1.176$ eV) lies roughly 0.08 eV beneath $E_g^{ind} = 1.26$ eV [36] and its broad-brand emission region is centered at 0.83 eV.

The spectral structures of the excitonic regions of samples 1, 5 and 7, depicted in greater details in Figure 3.2, are usually composed of zero-phonon lines (ZPL) followed by phonon replicas (PR). At 2K, a single ZPL labelled 'A' is present for all three samples. A thorough interpretation of the ZPLs and PR of each samples, based on the temperature evolution of their PL spectra is presented in Tables 3.1 and 3.2 (phonons of an additional WS_2 synthetic sample, sample 6 is also described). Most of the phonon energies from the MoS_2, WS_2 and WSe_2 single crystals differ from those reported for TO and LO lattice phonons as well as from other phonon active modes measured by IR and Raman spectroscopy [37, 38, 39, 40]. These phonons can be interpreted as local modes induced by the impurity centers which provide exciton related luminescence.

The broad-band regions of sample 1 and 5 are also enhanced in Figure 3.3 and reveal some structures at low temperature. The peaks identified in the figure for each sample appear at constant intervals and have been attributed to phonon replicas of a single dominant energy phonon mode (P_{bb}). Both modes are given in Tables 3.1 and 3.2. The two spectra were taken using two different experimental setups (see Table 2.2) with different resolutions which explains the 'choppy' structure of sample 5. Since the PL measurements were not performed under vacuum, some atmospheric absorption lines are also observed on the lower end of the broad-band emissions of both samples. Due to insufficient data, the broad-band of sample 7 could not be properly analyzed.

The two radiative regions were also observed in the other synthetic single crystals grown by vapor transport with a halogen gas agent (samples 2,3 and 6). The peaks in the excitonic regions of MoS_2 sample 2 and 3, which were grown with chlorine, corresponded

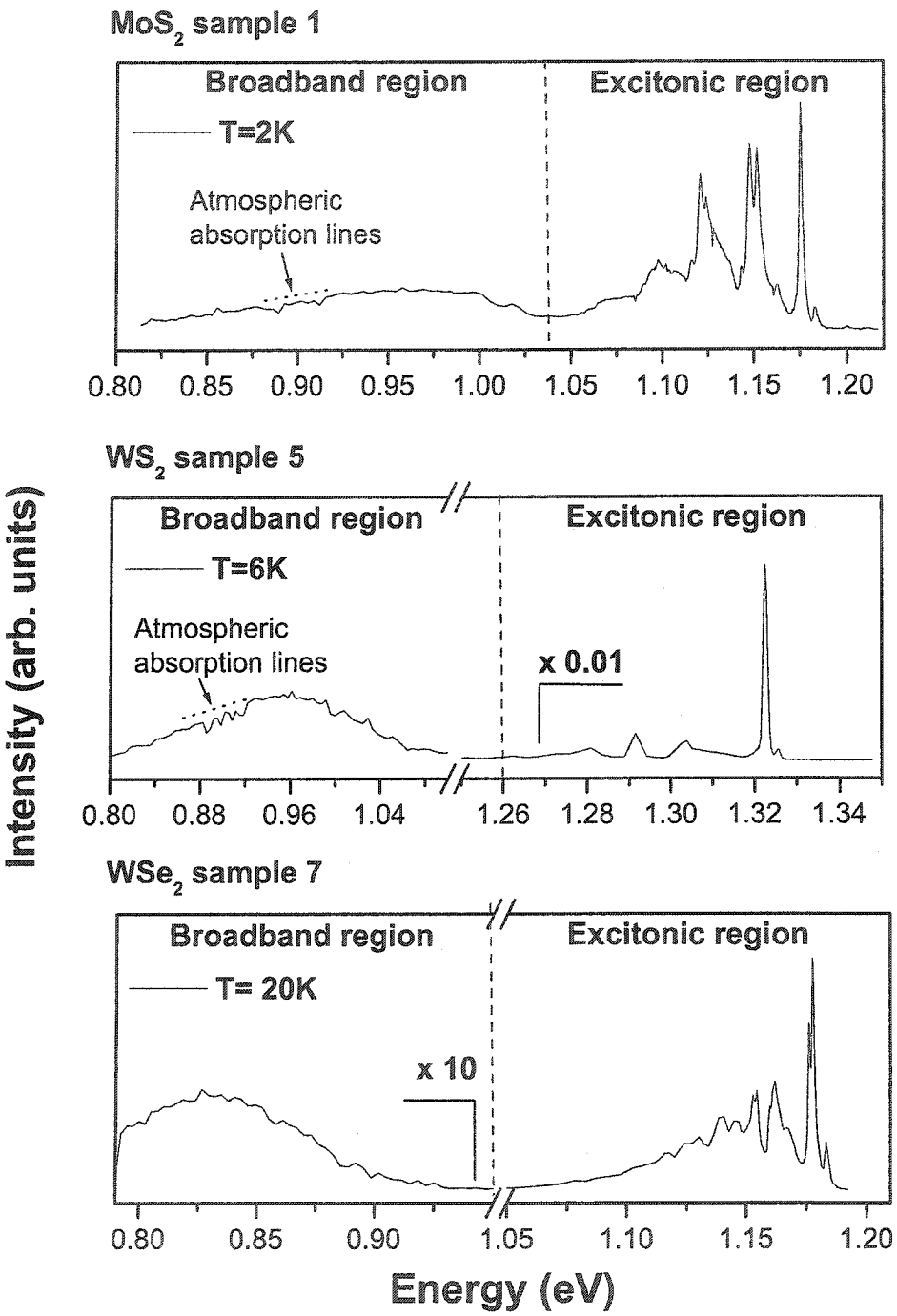

Figure 3.1: The characteristic spectra of sample 1, 5 and 7 at temperatures 2K, 6K and 20K respectively are presented. Two distinct radiative emission regions are observed for each samples: the excitonic and broad-band sections.

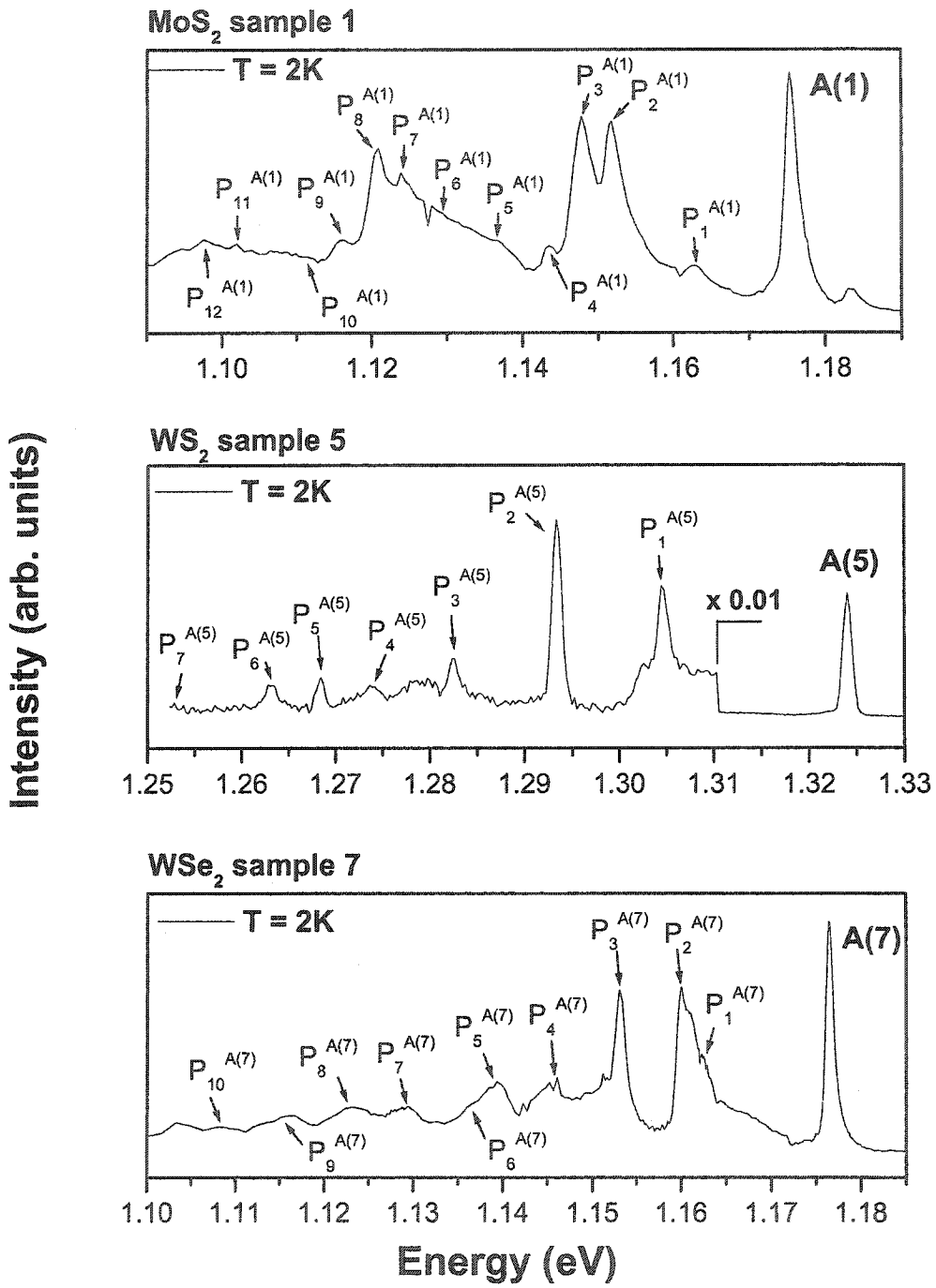

Figure 3.2: At 2K, excitonic regions for samples 1, 5 and 7 are comprised of a single zero-phonon line (ZPL) 'A' and several phonon replicas. Refer to Tables 3.1 and 3.2 for analysis.

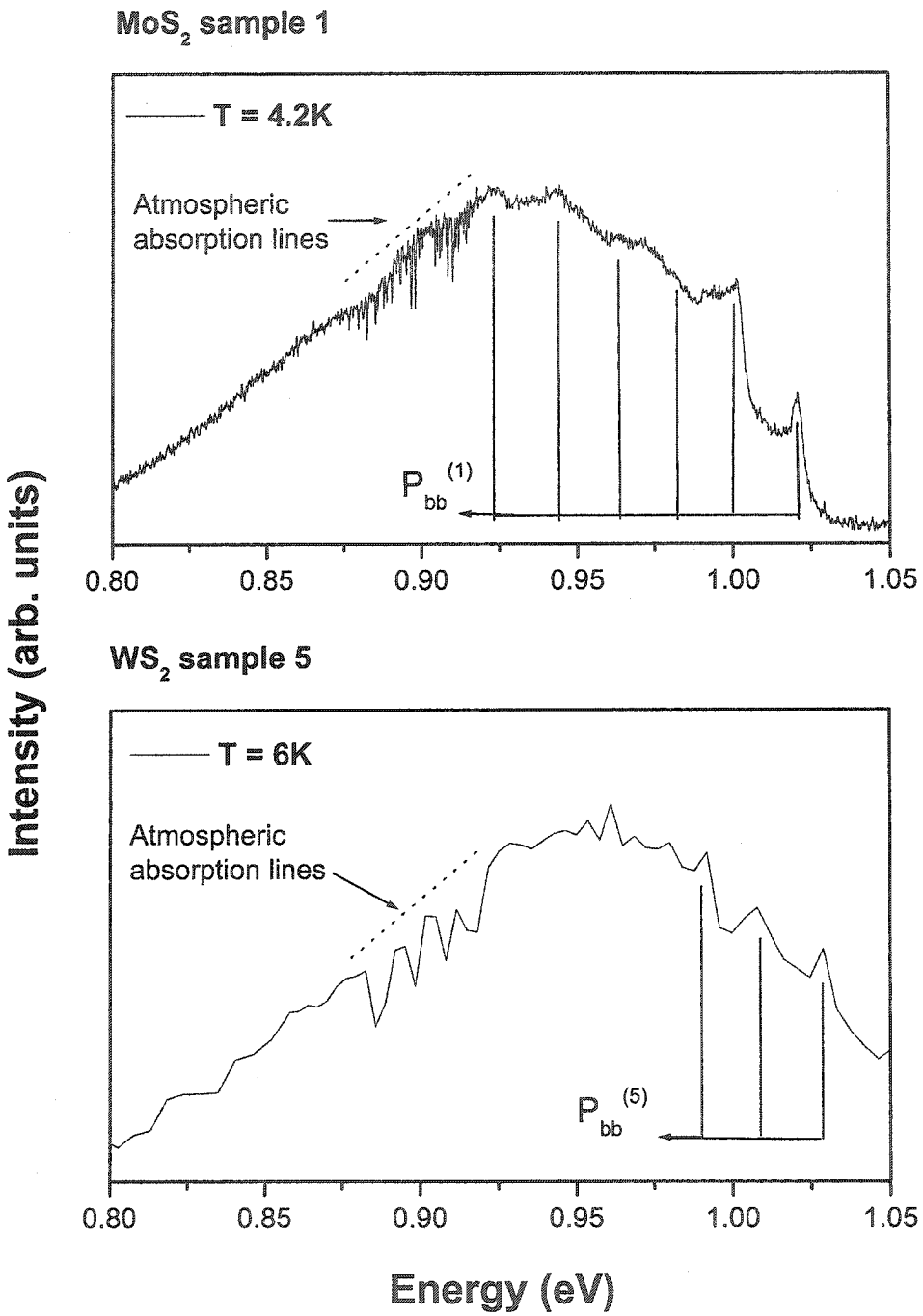

Figure 3.3: The 4.2K and 6K broad-band spectra of samples 1 and 5 respectively are illustrated. The dominant single phonon energy mode (P_{bb}) for both broad-bands were calculated by subtracting two consecutive peaks. The two PL spectra were taken with different PL setups and therefore at different resolutions.

exactly to the ones in sample 1 while the peaks from WS_2 sample 6, grown by iodine as opposed to bromine, were much broader than the ones from sample 5 and slightly shifted in position. The broad-band region was also observed in all three synthetic samples. The PL spectrum of the natural MoS_2 single crystals did not reveal any excitonic region. Throughout the whole temperature range only the IR broad-band emission with the same spectral shape as that of the synthetic crystals was detected. The radiative properties in both synthetic and natural single crystals are temperature-dependent; the excitonic and broad-band PL spectral structures evolve as the temperature increases and become subject to a thermal quenching at high enough temperatures. A more detailed analysis on the temperature dependence of the PL will be presented in the following section.

MoS_2 sample 1			WSe_2 sample 7		
Zero-phonon lines (eV)					
A(1)=1.1753			A(7)=1.1764		
B(1)=1.1772			B(7)=1.1780		
C(1)=1.1874			C(7)=1.1834		
Phonon replicas (P) ($^{(*)}$ from ref. [37])					
Notation	Shift(meV)	Analysis	Notation	Shift(meV)	Analysis
P_1	14.2	local	P_1	13.6	local
P_2	23.8	local	P_2	16.5	local
P_3	27.6	local	P_3	23.4	local
P_4	32.0	local	P_4	30.2	P_1+P_2
P_5	40.6	$A_g(M_{1+})^{(*)}$	P_5	37.8	$2P_3$
P_6	46.2	P_1+P_4	P_6	39.9	P_2+P_4
P_7	50.7	$A_{1g}(\Gamma_{1+})^{(*)}$	P_7	46.8	$2P_4$
P_8	55.2	$2P_3$	P_8	53.6	P_1+P_2+P_4
P_9	59.6	P_3+P_4	P_9	60.2	$2P_1$+$2P_2$
P_{10}	64.0	$2P_4$	P_{10}	68.0	P_5+P_6
P_{11}	72.6	P_4+$A_g(M_{1+})$			
P_{12}	79.0	$2P_3$+P_2			
Broad-band Phonon replica (meV)					
P_{bb} = 19.1			N/A		

Table 3.1: Peak assignments for MoS_2 and WSe_2 samples

WS_2 sample 5			WS_2 sample 6		
Zero-phonon lines (eV)					
A(5)=1.324			A(6)=1.326		
B(5)=1.327			B(6)=1.329		
C(5)=1.337			C(6)=1.339		
Phonon replicas (P) ((*) from ref. [37])					
Notation	Shift(meV)	Analysis	Notation	Shift(meV)	Analysis
P_1	19.5	local	P_1	11.4	local
P_2	30.7	local	P_2	18.7	local
P_3	41.6	local	P_3	30.3	local
P_4	50.2	P_1+P_2	P_4	41.7	P_1+P_3
P_5	55.6	local	P_5	55.6	P_1+E^1_{2g} (*)
P_6	61.1	P_1+P_3	P_6	60.6	$2P_3$
P_7	72.3	P_2+P_3			
Broad-band Phonon replica (meV)					
$P_{bb} = 21.0$			N/A		

Table 3.2: Peak assignments for WS_2 samples

3.2 PL temperature dependencies

3.2.1 Temperature evolution of the PL spectra

The temperature evolution of the excitonic PL from MoS_2 sample 1 is presented in Figure 3.4. The zero-phonon line and phonon replica sections have been separated to facilitate the analysis. There are at least three ZPLs contributing to the excitonic emission intensity. The first line, A ($E_A = 1.1753$ eV) can only be clearly seen at the lowest temperature of 2K (see Figure 3.2). Already at $T = 4.2$K the A line is not completely resolved and can only be perceived as a shoulder of the second zero-phonon line B ($E_B = 1.1772$ eV). At higher temperatures, the last ZPL C ($E_C = 1.1873$ eV) appears and becomes dominant at $T > 50K$. Increasing the temperature leads to the redistribution of the PL intensity starting from line A to line B, then from B to C. The phonon energy modes inscribed in Table 3.1 were carefully deduced from the temperature behavior of the phonon replica peaks. An energy mode was found when a phonon triplet (the A, B and C ZPLs replicas)

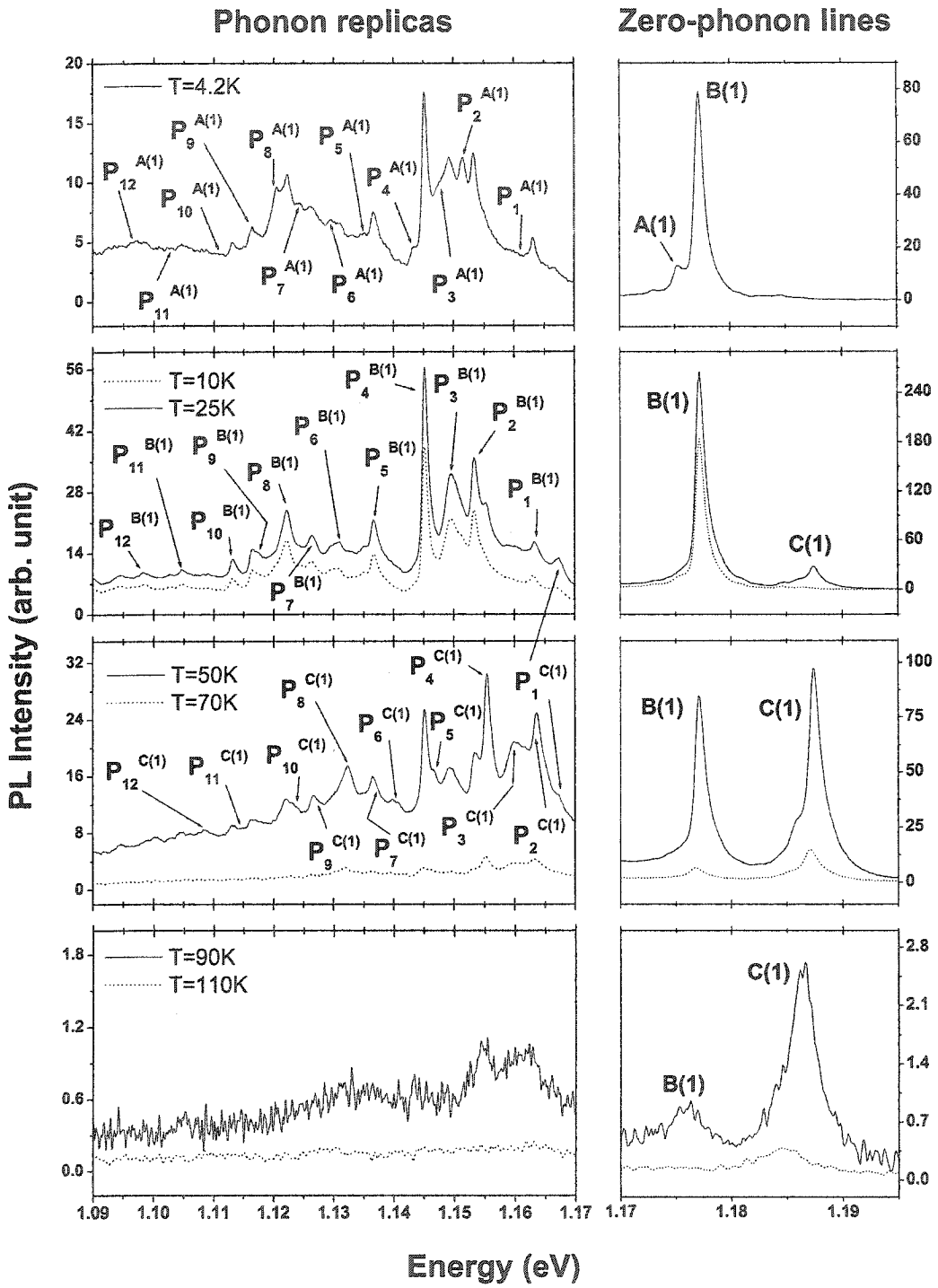

Figure 3.4: Temperature dependence of the excitonic region of the MoS_2 sample 1 taken at the NRC. The zero-phonon lines and phonon replicas are divided into two sections. The ZPLs and many of the PRs are labelled in Table 3.1

could be observed. While the main local phonon energy modes were easy to point out, the several secondary modes arising from interactions between local modes and even lattice active modes were much harder to distinguish due to the phonon peaks overlapping with each other. It was therefore not possible to label all of the peaks illustrated in the PL spectra.

Taking a closer look at the ZPL section in Figure 3.4, one may observe several substructures between the B and C lines as well as within their extremities. A comparative study between MoS_2 sample 1, 2 and 3 (not shown) revealed that these sharp lines exist in all three synthetic crystals and are designated as weaker ZPLs.

Figures 3.5 and 3.6 illustrate the excitonic temperature evolution of the WS_2 synthetic crystals (samples 5 and 6) and WSe_2 crytals (sample 7) respectively . As previously mentioned, sample 5 was grown using bromine as the transport agent while sample 6 used iodine. Their excitonic radiative transitions occur in the same near-infrared region and have similar spectral structure and temperature behavior. However because of the relatively large width of the spectral components, the A and B ZPLs as well as their phonon replicas are not resolved in sample 6. The excitonic peak assignments for both samples are given in Table 3.2.

Apart from differences in peak positions and line intensities, all synthetic single crystals studied have essentially the same excitonic PL spectral structure and temperature evolution. All samples have three major zero-phonon lines (A,B and C) as well as phonon replicas created by the local vibronic modes of the radiative centers. The PL intensity redistribution is also played out in the same manner for all samples as well: A to B and then B to C. Finally, a similar abrupt thermal quenching of the PL intensity at higher temperatures also occurs in all three samples.

Turning now to the second radiative region, Figure 3.7 depicts the temperature evolution of the broad-band emission of sample 1. From the 2K to 70K temperature range, the spectral structure of the broad-band remains relatively constant with the exception of the gradually vanishing phonon replica peaks as the temperature increases. A similar temperature behavior was also observed for the broad-band region of sample 4 as well as for the WS_2 sample 5 and is expected to occur for all broad-band regions of the synthetic and natural single crystals. Beyond T= 90K, a thermal quenching process, similar to one observed for the excitonic region, also occurs.

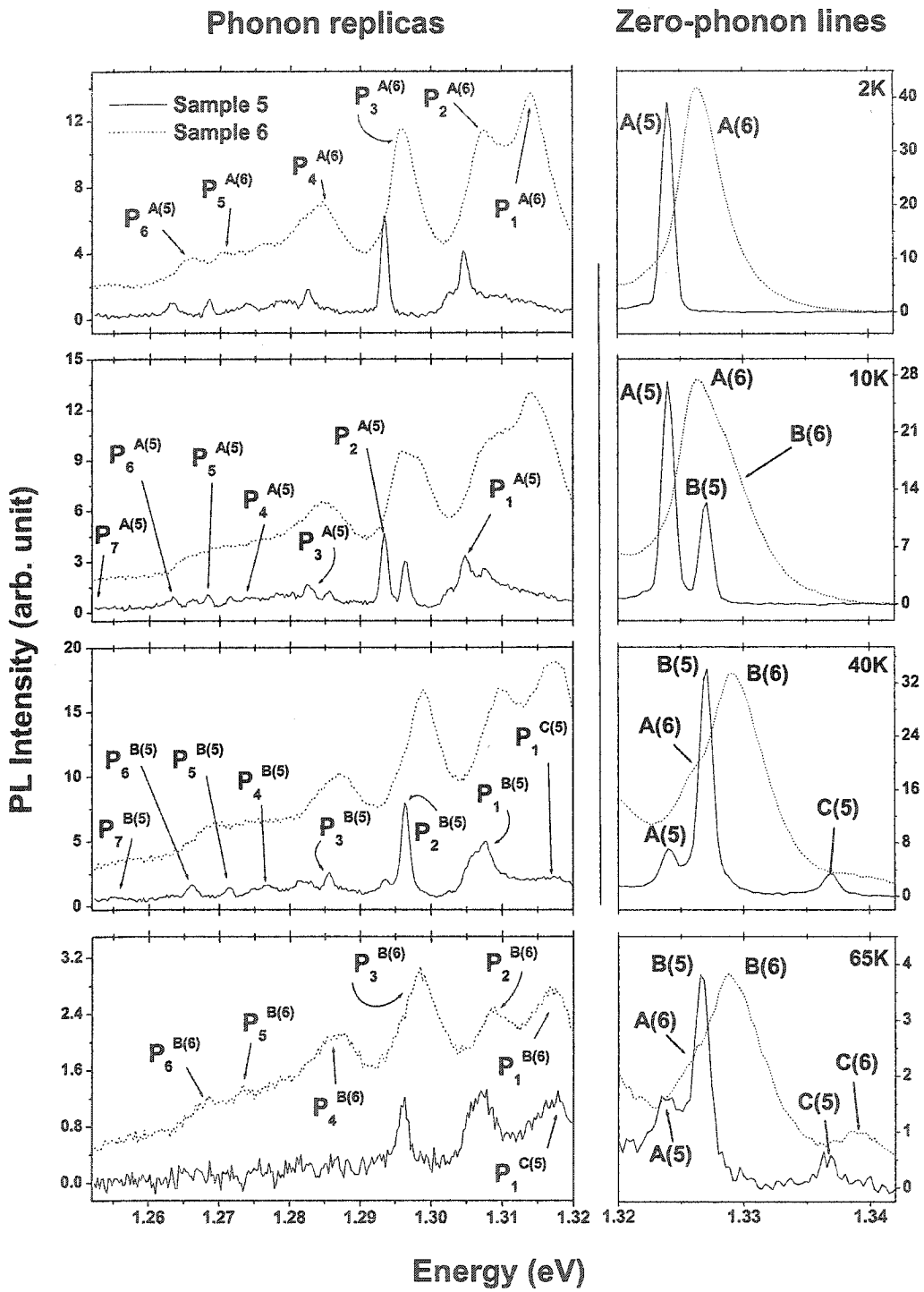

Figure 3.5: Temperature evolution of the excitonic regions of WS_2 sample 5 and 6. Please refer to Table 3.2 for analysis.

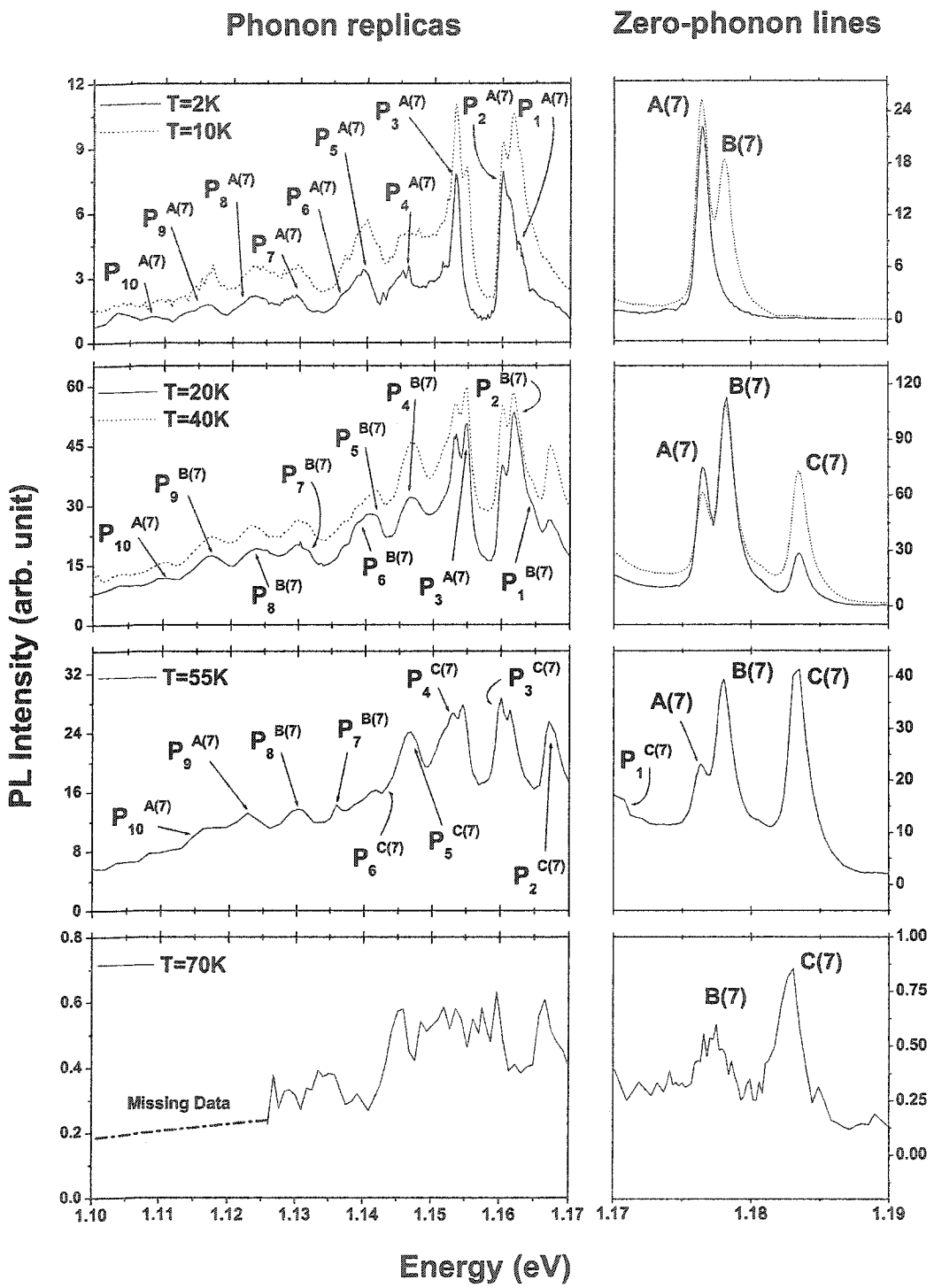

Figure 3.6: Temperature evolution of the excitonic region of WSe_2 sample 7. Please refer to Table 3.1 for analysis.

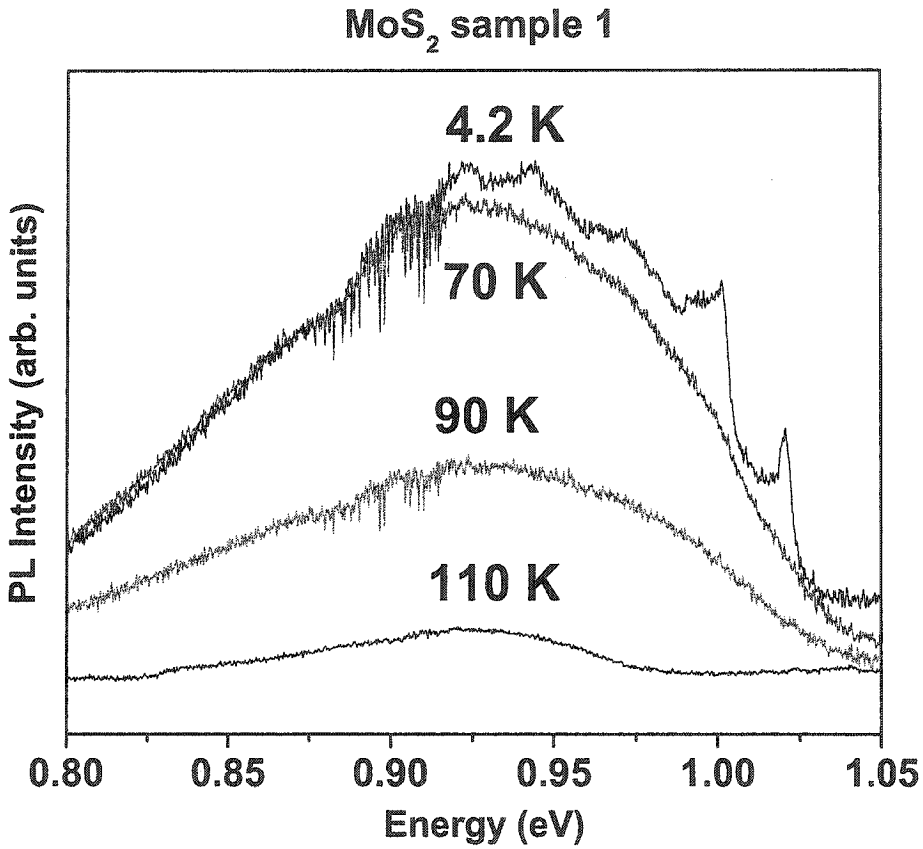

Figure 3.7: The temperature evolution of the broad-band PL spectrum of MoS_2 sample 1. and its integral PL intensity. The activation energy of the thermal quenching process is calculated with Eq. 1.12.

3.2.2 Thermal quenching process

At higher temperatures, the radiative emissions from the excitonic and broad-band regions are subjected to a thermal quenching process which has been implicitly observed in the temperature evolution PL spectra of section 3.2.1. Plotting the ZPL integral PL intensity $I_{ex}(T)$ and broad-band integral PL intensity $I_{bb}(T)$ as a function of temperature in Figure 3.8 provides a more accurate picture of the thermally activated processes occurring in both regions. While the excitonic quenching takes place in the same temperature range for all three samples, the broad-band quenching occurs at a much higher temperature. This difference suggests two distinct thermal processes. A slight augmentation of the $I_{bb}(T)$ (encircled in Figure 3.8) is observed just before the thermal quenching occurs and will be discussed in greater details in section 3.5. Notwithstanding the increase in excitonic integral PL intensity at low temperatures in samples 1, 5 and 7 (which will also be dealt with in section 3.5), the temperature behavior of $I_{ex}(T)$ and $I_{bb}(T)$ in Figure 3.8 can be adequately described by the Mott-Seitz formula, Eq. 1.12. Table 3.3 provides the activation energy values E_{qx} and E_{qbb} of the thermal quenching mechanisms as well as the constants $C_{qx,qbb} = \tau_{Rx,Rbb}/\tau_{Nx,Nbb}$ used to fit Eq. 1.12 to the experimental points.

Parameters	MoS_2 sample 1	WS_2 sample 5	WSe_2 sample 7
E_{qx}	0.116	0.125	0.084
E_{qbb}	0.17	–	–
C_{qx}	$\sim 1E9$	$\sim 1E10$	$\sim 1E8$
C_{qbb}	$\sim 1E8$	–	–

Table 3.3: Parameters of Eq. 1.12 for different samples.

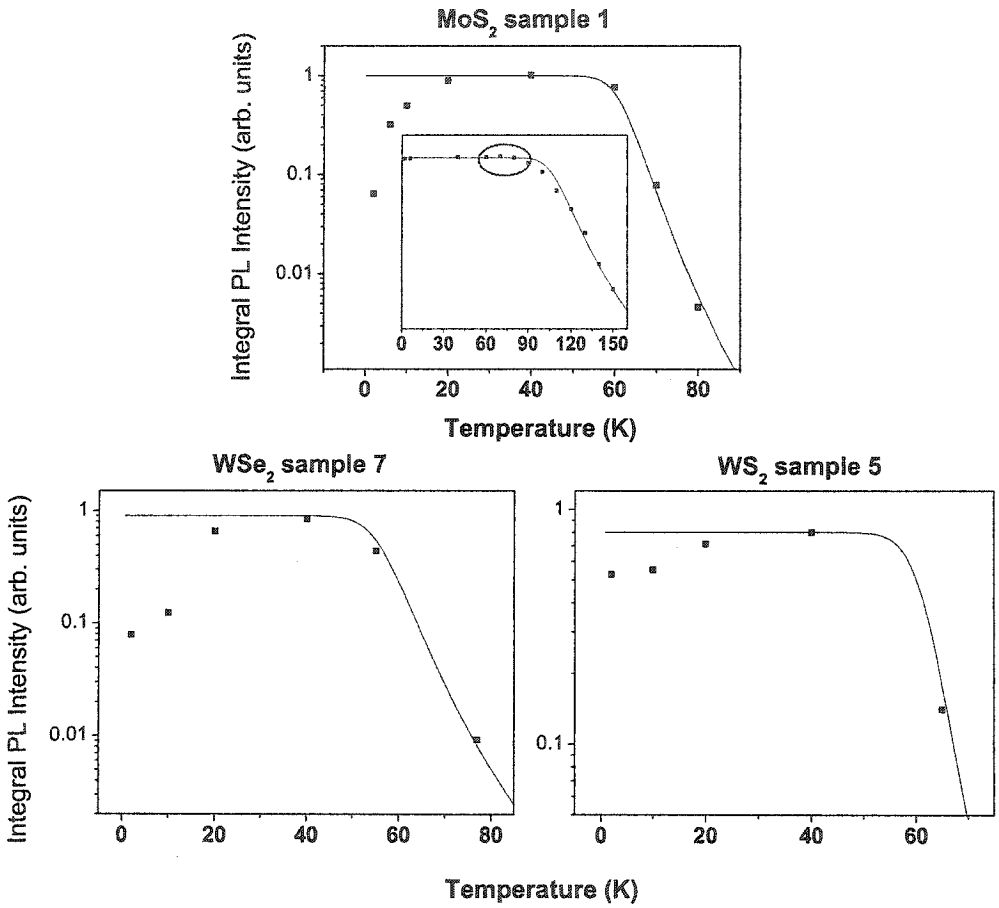

Figure 3.8: The temperature dependence of the total ZPL integral PL intensity ($I_{ex}(T)$) of samples 1, 5, and 7 is presented. The broad-band integral PL intensity ($I_{bb}(T)$) is also shown for sample 1. The activation energies of the thermal quenching processes is calculated for each sample by fitting Eq. 1.12 to the experimental data. The circled area displays a small increase in the $I_{bb}(T)$ which will be explained in greater detail in section 3.5.

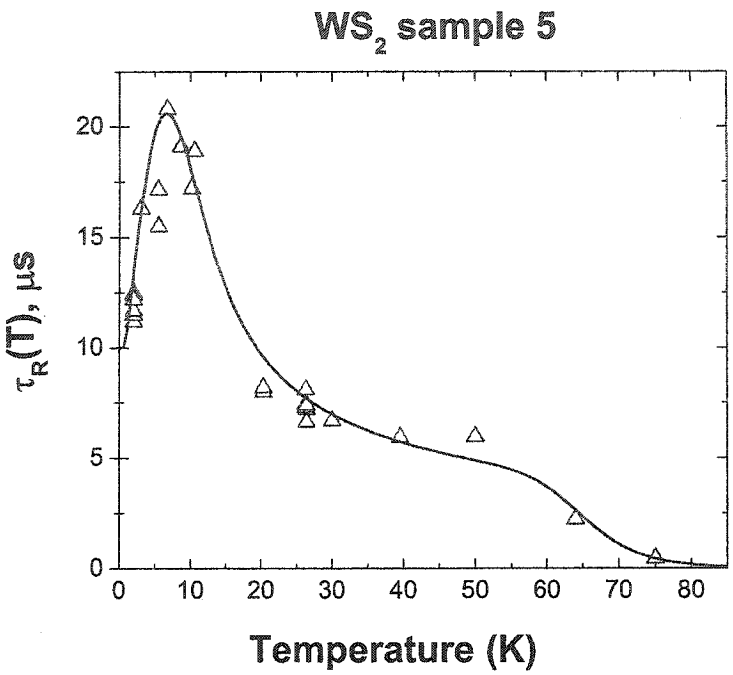

Figure 3.9: Temperature dependence of the ZPL PL time-decay for WS_2 sample 5. The theoretical fit of the experimental data points is given by Eq. 1.15 from section 1.4.1.

3.3 Time-resolved measurements

The temperature evolution of the excitonic ZPLs PL decay time for the WS_2 sample 5 was also studied. The temporal decay was observed to be exponential throughout the temperature range of 2K-70K. As seen in Figure 3.9, the time decay increases quite rapidly at low temperatures before reaching its maximal value of $\approx 20\mu s$ at T=7K. The radiative life-time then gradually decreases to about $6\mu s$ before a fast quenching process occurs, possibly caused by the same thermal quenching observed in the steady state PL spectrum (see Figure 3.8). The experimental temperature dependence of the time decay was described by Eq. 1.15 taken from the multi-level system model in section 1.4.1 and will be discussed in section 3.5. The radiative life-times for the excitonic PL were not measured for the WSe_2 crystals nor for the synthetic MoS_2 samples, which in that case could not be experimentally determined because of the slow response ($\sim$ 30msec) of the cooled Ge detector.

3.4 Origins of the PL emissions and their thermal quenching

3.4.1 Excitonic PL

The spectral distribution and temperature dependence of the sharp spectral lines in the synthetic MoS_2, WS_2 and WSe_2 single crystals are very similar in behavior to the excitonic multiplets caused by the electron-hole *j-j* coupling well-known for silicon, some III-V materials and II-VI semiconductors with isoelectronic impurities [22, 41, 42]. However in contrast to isoelectronically doped GaP or Si, where in the absence of external perturbations [43, 44, 45, 46] the *j-j* coupling are manifested as a so-called $A-B$ spectral doublet, the excitonic spectra of the layered transition metal dichalcogenide MoS_2, WS_2 and WSe_2 involve three major zero-phonon lines (A,B and C). The luminescent properties of these crystals can thus be attributed to the radiative recombination of excitons bound to neutral centers, which exhibit in 2H-TX_2 layered compounds the same properties as the isoelectronic traps in GaP and Si, resulting in efficient luminescence in indirect band gap semiconductors.

The impurity centers in the transition metal dichalcogenides which will now be identified as T_1 were assumed to originate from the diatomic halogen molecules (Cl_2 for MoS_2, I_2 or Br_2 for WS_2 and WSe_2) unambiguously positioned within the van der Waals gap. Because of their large electronic affinity, the neutral halogen molecules arranged between the $X-T-X$ sheets can exhibit properties of electron-attractive centers [47], creating a short-range potential similar to that of the isoelectronic traps in GaP. Although several papers observed traces of halogen in the crystals grown by vapor transport method [48, 49, 50], none indicated where the halogens were positioned inside the lattice. Therefore an in depth analysis of the common lattice structure shared by the MoS_2, WS_2 and WSe_2 crystals illustrated in Figure 3.10 (A) was first performed to study the feasibility of the halogen molecules intercalating within the layers of the crystals. Geometrical calculations using the well-known lattice parameters [1, 51, 52] shown in Table 3.4 have revealed a very good match between the halogen molecules and the interstitial space of two adjacent triangular pyramids (quasi-tetrahedral), formed by sulfur or selenium atoms, found in the host crystalline lattice's van der Waals gap. Figure 3.10 (B) illustrates a sphere of radius r_{cal} that can be fitted in the triangular pyramid for the MoS_2, WS_2 and WSe_2 single crystals. It can be seen from Table 3.4 that the r_{cal} values are very close to the halogen atomic radii of chlorine, bromine and iodine and that the distances between the

T and X covalent radii[1]	$r_S = 1.02$	$r_{Se} = 1.16$	Å
	$r_{Mo} = 1.45$	$r_W = 1.46$	
halogen covalent radii[1]	$r_{Cl} = 0.99$	$r_{Br} = 1.14$	$r_I = 1.33$
lattice parameters[2]	MoS_2	WS_2	WSe_2
a	3.160	3.153	3.286
c	12.294	12.323	12.965
α	3.47	3.53	3.67
calculated values			
r_{cal}	1.020	1.034	1.124
t-t	2.145	2.128	2.220

[1] from ref. [52]

[2] from ref. [1, 51]

Table 3.4: Lattice Parameters and atomic radii

centers of the pyramids with a common lateral side $(t - t)$ are also well-matched for the diameters of the halogen molecules. Consequently, as depicted in Figure 3.10 (C), it is possible that an effective intercalation of the gaseous transport agent into the layered crystal during growth process can occur.

It should be noted that in some cases, where the halogen atomic radii are larger than r_{cal}, the intercalation induces small distortions in the host lattice and therefore modifies the radiative properties. Figure 3.5 illustrates spectral lines almost 10 times larger in sample 6 than those of sample 5. Such a difference is a direct consequence of the greater distortion upon the WS_2 host lattice induced by the larger intercalated iodine molecules in sample 6 as opposed to the smaller bromine molecules in sample 5. WSe_2 sample 7 was also grown with iodine, however since the interlayer distance of the WSe_2 lattice is greater than WS_2, the distortion produced was not as great and therefore no broadening of the spectral lines occurred.

Finally, the absence of the excitonic luminescence in the natural MoS_2 samples and in WSe_2 synthetic single crystals grown without halogen transport agent [19] confirmed the assumption that the radiative excitonic PL was indeed due to the halogens molecules.

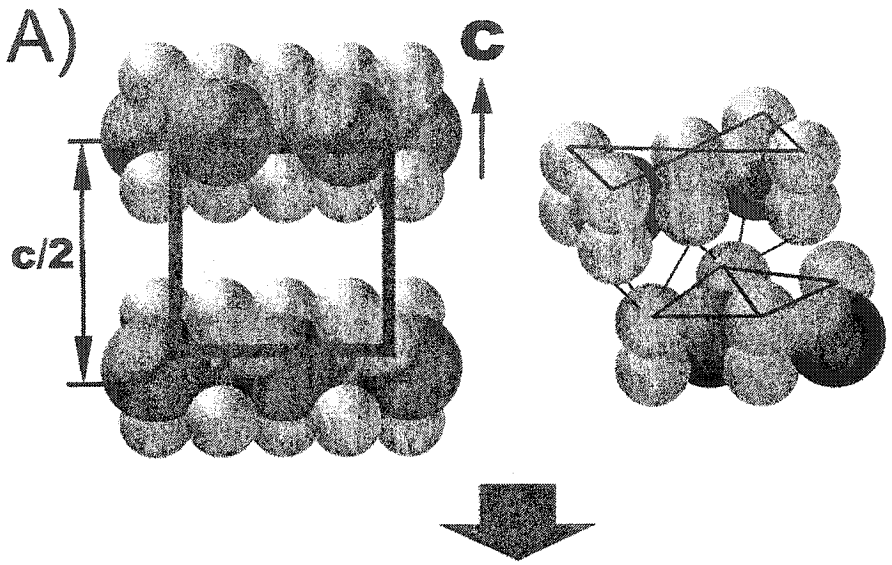
A)
c
c/2

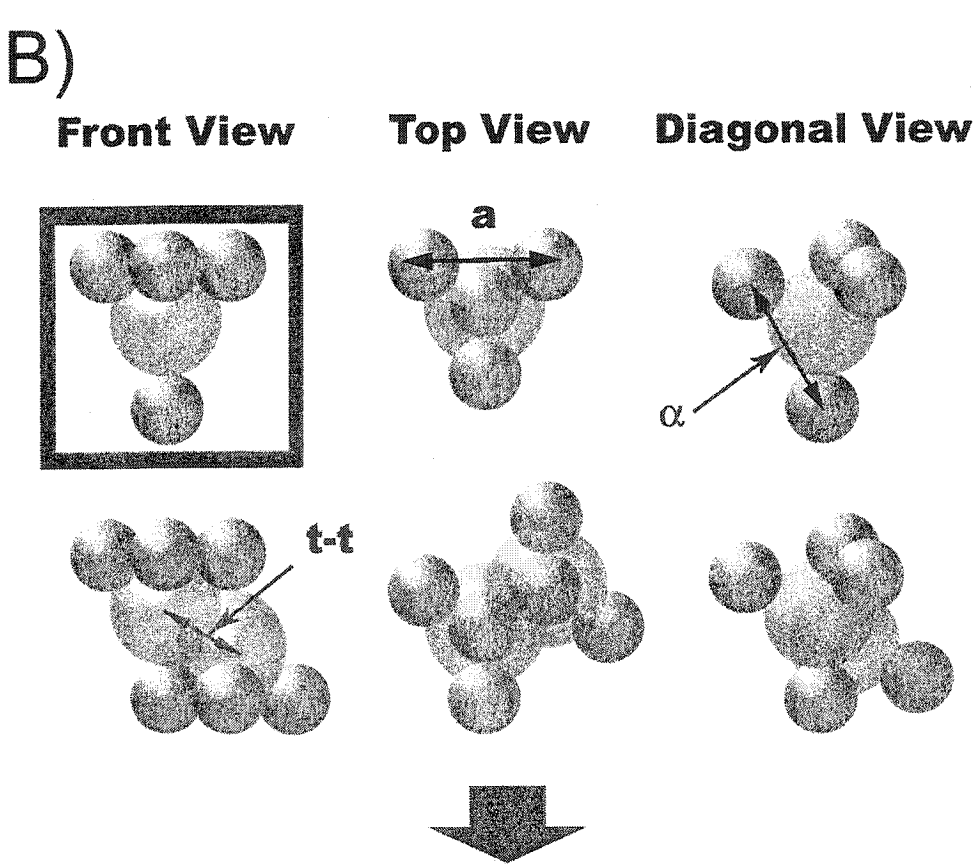
B)
Front View
Top View
Diagonal View
a
α
t-t

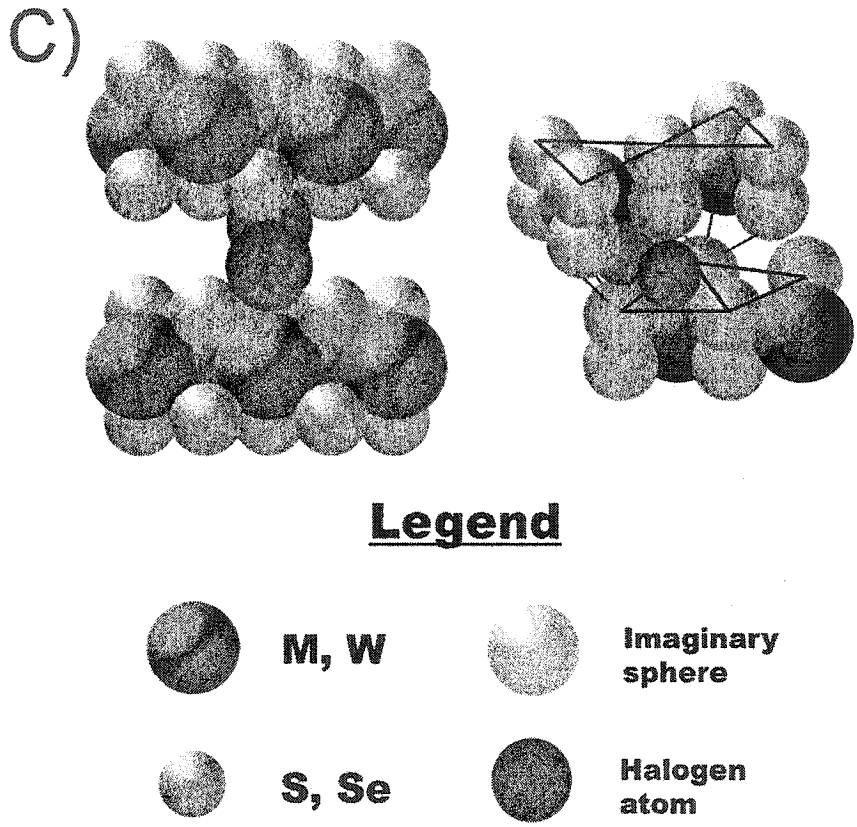

Figure 3.10: (A) displays a front and diagonal view of the TX_2 (T=Mo,W;X=S,Se) transition metal dichalcogenide hexagonal crystal lattice structure where c/2 is the T-T distance in the unit cell. (B) illustrates the largest imaginary sphere with radius r_{cal} which can be incorporated in a triangular pyramid in the van der Waals gap where a is the X-X distance in the plane perpendicular to c, α is the least interlayer X-X distance and t-t is the calculated distance between the centers of two adjacent triangular pyramids. (C) presents the same two views of the lattice structure from A) with the intercalated halogen molecules.

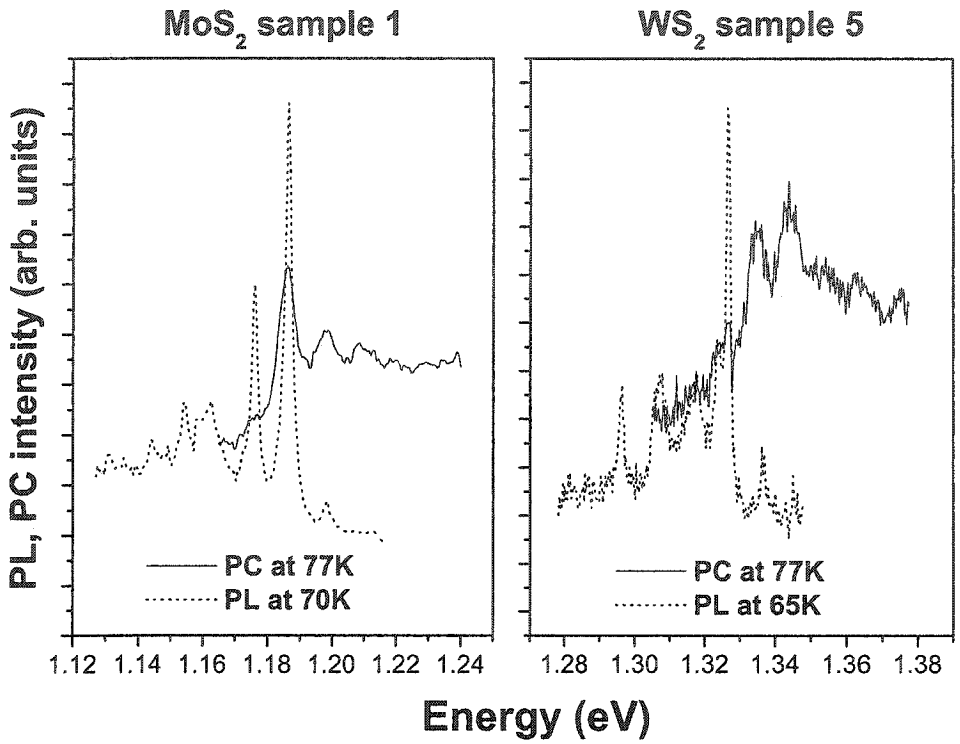

Figure 3.11: PC and PL spectra for samples 1 and 5.

Photoconductivity measurements on the synthetic and natural MoS_2 (sample 1 and sample 4) and the WS_2 crystal (sample 5) also confirmed the assumption that the halogen molecules were positioned between the layers of the crystals. Although both electrode configurations (see section 2.3) permitted the observation of the well-known intrinsic free exciton transitions [1, 53] in all three crystals, the sandwich configuration was the only one which revealed sharp structures in the infrared region and that, only in the MoS_2 and WS_2 synthetic samples. The good agreement between the PC peaks from both synthetic samples and the ones observed in the PL spectra shown in Figure 3.11 confirms the PC and PL structures originate from the same halogen impurity complexes. The observation of the bound excitons exclusively in the sandwich electrode configuration for the synthetic samples indicates an extrinsic origin of the near infrared structures located within the layers of the material.

3.4.2 Broad-band PL

The spectral shape and temperature behavior of the broad-band observed in the MoS_2, WS_2 and WSe_2 single crystal samples suggest that this emission occurs as a result of radiative transitions between a deep donor center (now referred as T_2) associated with an intrinsic defect of the crystal lattice and the valence band in the conditions of a strong electron-phonon coupling [45, 54, 55]. As mentioned in section 3.1, the several peaks observed in that spectral region at low temperature for the MoS_2 and WS_2 samples can be attributed to the phonon replicas of a single zero-phonon radiative transition. The broad-band electronic zero-phonon line energetic position 1.039 eV and 1.050 eV for MoS_2 and WS_2 respectively can be obtained by adding the energy of the local vibronic mode to the first peak observed in Figure 3.3 for each sample. As discussed in section 1.3.4, as the electron-phonon coupling increases the zero-phonon radiative emission decreases. Therefore due to the strong coupling, the ZPL of the broad-bands cannot be observed in the PL spectra.

3.4.3 Thermal quenching processes

It is necessary to identify the origins of the fast thermal PL quenching processes seen in Figure 3.8, to which the radiative emissions are subjected. As mentioned in section 3.2.2, the different activation energies of the thermal processes for the excitonic and broad-band regions suggest two separate quenching mechanisms. Taking the difference between the indirect gap energy and the energetic position of the excitonic region ($E_g^{ind} - E_{ex}$) for samples 1, 5 and 7, we obtain values very similar to the excitonic activation energies found in Table 3.3. This equality suggests that the abrupt excitonic quenching is caused by the thermal depopulation of the electron-attractive impurity centers T_1 rather than by a nonradiative multiphonon recombination process, which is the case for the deep center T_2 [55]. The thermal depopulation of the centers observed in steady-state PL spectra stems essentially from the same single thermally activated process described by Eq. 1.15 for the time-decay model.

3.5 Models and diagrams

This section will apply the models introduced in chapter 1 to the experimental data. The first part will consist in applying the multi-level system model from section 1.4.1 to the temperature evolution of the excitonic PL time decay for the WS_2 sample 5. Next, the

integral PL intensity measurements of samples 1, 5 and 7 as a function of temperature will be described by the kinetic recombination model from section 1.4.2. Finally, a configuration coordinate diagram, presented in section 1.4.3, will be constructed for the MoS_2 synthetic single crystals using the data acquired from steady state measurements.

3.5.1 Time-decay model

Before applying the time-decay model, a qualitative analysis of the decay time temperature evolution from section 3.3 will first be given in terms of the PL spectra temperature evolution. As seen in section 3.2.1, the ZPLs PL intensity is redistributed to higher energetic lines as the temperature increases (A to B then B to C). This behavior indicates that the transition probabilities of the upper excitonic states are higher than the lower ones (i.e. their respective radiative life-times are shorter). As a result, the PL intensity contribution of the higher energy lines increases with their thermal population. Returning to time-resolved measurements, one should expect to see in Figure 3.9 a continuously decreasing time-decay value with rising temperature. However this is not the case as the time-decay value actually increases between 2K and 7K. This escalating decay time occurs while the PL spectra exhibit only the lower energy A-line suggesting the existence of an additional excitonic state (A') with a much longer radiative life-time between the A and B lines. Due to its long radiative life-time, A', while already populated at very low temperatures, does not contribute to the steady-state spectrum. Therefore, A' can only be detected in the time-resolved temperature evolution measurements.

Taking into account the new long life-time A' excitonic state, a four level time-decay model may now be constructed (see figure 3.12) and applied to the experimental data. The best fit of Eq. 1.15, obtained with: $\tau_A = 10\mu s$, $\tau_{A'} \geq 1ms$, $\tau_B = 2.5\mu s$, $\tau_C \cong 0.5\mu s$, $\Delta_{A'A} = 0.3$ meV, $E_a = 0.1$ eV, $g_A = g_C = 1$ and $g_{A'} = g_B = 2$, is illustrated in Figure 3.9. The energy values of $\Delta_{AB} = 3.0$ meV, $\Delta_{AC} = 13$ meV were taken from the steady-state spectra. It should be noted that the shape of the calculated time-decay temperature dependence was not seriously affected by the A' level life-time for values greater than 1ms. The energy E_a of the thermally activated process was taken to be approximately the same as for the steady-state PL thermal quenching. As for the preexponential factor τ_0^{-1}, it was appointed equal to the frequency of the most prominent local vibronic mode $P_2^{(5)}$: $\tau_0^{-1} \approx 1 \times 10^{13} s^{-1}$.

As previously stated, time-resolved measurements were not performed on MoS_2 sample 1 and WSe_2 sample 7. Although there is no way to know of the possible existence of

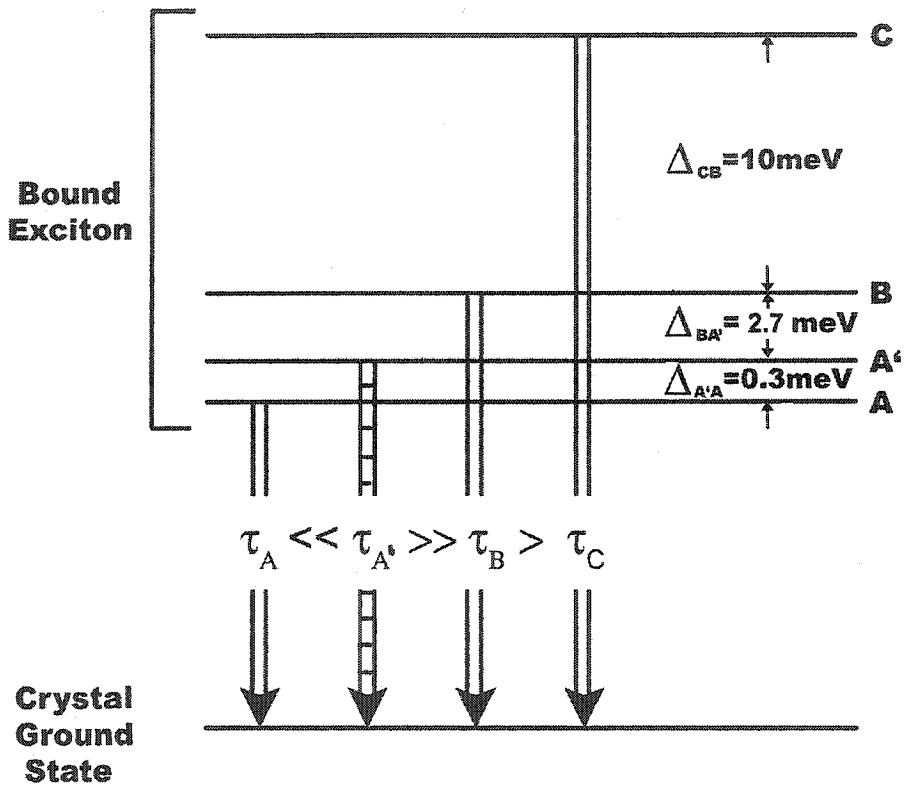

Figure 3.12: Four level model describing the temperature evolution of the decay time of WS_2 sample 5.

nonradiative levels (long life-time) such as A' in sample 5 without taking experimental time-resolved measurements, some useful information on the decay times of the *radiative* levels may yet be extracted from the steady-state PL spectra taken at different temperatures. As stated in [56], without direct measurements, the ratio of the life-times of the A,B and C lines may be derived using integral PL intensity ratios given by:

$$I_i/I_j = N_i^x \tau_j / N_j^x \tau_i \tag{3.1}$$

where $I_{i,j}$ is the line intensity of the i-th or j-th states, $N_{i,j}^x$ is the exciton concentration and $\tau_{i,j}$ is the lifetime. Inserting Eq. 1.14 into 3.1 and assuming thermal equilibrium, the integral PL intensity ratios of line A,B and C can be represented by:

$$I_B/I_A = g_{BA} \cdot (\tau_A/\tau_B) \cdot exp(\Delta_{BA}/kT) \tag{3.2}$$

$$I_C/I_B = g_{CB} \cdot (\tau_B/\tau_C) \cdot exp(\Delta_{CB}/kT) \tag{3.3}$$

where $g_{BA} = g_B/g_A$ and $g_{CB} = g_C/g_B$. From steady-state PL spectra, the integral PL intensities of the lines as well as the energy values Δ_{BA} and Δ_{CB} were measured. Fitting Eqs. 3.2 and 3.3 to the experimental integral PL intensity ratios as a function of temperature yielded $g_{BA} \cdot (\tau_A/\tau_B) \cong 250$ and $g_{CB} \cdot (\tau_B/\tau_C) \cong 8$ for sample 1. Although the life-times may not be measured directly since g_{BA} and g_{CB} are unknown, it is clear from the ratios that $\tau_A \gg \tau_B > \tau_C$. The same procedure was applied to sample 7 and generated values of $g_{BA} \cdot (\tau_A/\tau_B) \cong 15$ and $g_{CB} \cdot (\tau_B/\tau_C) \cong 6$. Eqs. 3.2 and 3.3 were also fitted in the same manner to the experimental integral PL intensity ratios of sample 5. The values found were in very good agreement with the assigned time decay and level degeneracy values previously mentioned, confirming the validity of the technique.

3.5.2 Kinetic recombination model

The temperature evolution of the excitonic and broad-band integral intensity measurements from section 3.2.2 will now be described by the kinetic recombination model previously formulated in section 1.4.2. According to the model, the radiative emission is played out through two distinct channels. The first channel, created by the electron-attractive halogen molecule centers T_1, permits bound exciton radiative recombination via a certain number of levels (in this case A,B and C). The second channel, originating from the lattice defect-induced deep centers T_2, also allows radiative recombination and

acts as a shunt path, competing with the T_1 channel.

Parameter Calculation

The radiative recombination intensity of both channels as a function of temperature, given by Eqs. 1.20 and 1.21, is dependent on the life-times $\tau_{Rx}(T)$, $\tau_{cp}(T)$, $\tau_{xp}(T)$, τ_{Nx}, τ_{Rbb}, and τ_{Nbb}.

The life-times (and their parameters) needed to construct the theoretical curves of the kinetic recombination model will now be obtained for MoS_2 sample 1, WS_2 sample 5 and WSe_2 sample 7. It should be noted that not all experimental measurements were performed on each crystal therefore, due to the strong similarities between the samples, some of the unknown parameter values were determined based on experimentally measured values of other samples.

$\tau_{Rx}(T)$, the radiative lifetime temperature dependence may be expressed with Eq. 1.23 instead of Eq. 1.15 since the thermally activated mechanisms are already taken into account in the kinetic recombination model. Seeing as all three samples have three radiative levels (A,B and C), Eq. 1.23 may be rewritten in the more explicit form of a 3-level system

$$\tau_{Rx}(T) = \frac{\tau_A \cdot (1 + g_{BA} \cdot exp(-\Delta_{BA}/kT) + g_{CA} \cdot exp(-\Delta_{CA}/kT))}{1 + g_{BA} \cdot (\tau_A/\tau_B) \cdot exp(-\Delta_{BA}/kT) + g_{CA} \cdot (\tau_A/\tau_C) \cdot exp(-\Delta_{CA}/kT)} \quad (3.4)$$

$$= \frac{\tau_A \cdot (1 + g_{BA} \cdot exp(-\Delta_{BA}/kT))(1 + g_{CB} \cdot exp(-\Delta_{CB}/kT))}{(1 + g_{BA} \cdot (\tau_A/\tau_B) \cdot exp(-\Delta_{BA}/kT))(1 + g_{CB} \cdot (\tau_B/\tau_C) \cdot exp(-\Delta_{CB}/kT))} \quad (3.5)$$

This equation is valid for all three samples. The contribution of the radiative recombination intensity is assumed to come solely from the radiative excitonic levels (A,B and C). Therefore all nonradiative levels, such as the A' level of sample 5, have been neglected. Most of the parameters of Eq. 3.5 for samples 1, 5 and 7 were calculated in section 3.5.1. While τ_A,τ_B and τ_C as well as the degeneracy values g_{BA} and g_{CB} were directly calculated for sample 5, life-times ratios $g_{BA} \cdot (\tau_A/\tau_B)$ and $g_{CB} \cdot (\tau_B/\tau_C)$ were used as an alternative for samples 1 and 7. Identical g_{BA} and g_{CB} values from sample 5 were given to sample 1 and 7. The τ_A values for sample 1 and 7 were evaluated under

the assumption that the radiative life-time of the B-line transition for both crystals was of the same order of magnitude as in sample 5.

$\tau_{cp}(T)$ and $\tau_{xp}(T)$, given by Eqs. 1.22 and 1.26 respectively, were calculated using Eqs. 1.24 and 1.25. The values of N_C, N_V and ν_{th} were evaluated assuming $m_e = m_h = m_0$ (m_0 being the free electron mass) for all three samples [57, 58, 59]. σ_{px} was estimated using similar values for isoelectronic centers in GaP [26, 28, 60, 61]. N_{T1} was adjusted taking into consideration that the concentration of halogen molecules was relatively low. Hall measurements were performed on sample 5 [62], revealing that the majority carrier concentration n_0, essentially constant for $T < 150$K, is approximately $10^{10} \sim 10^{11}\text{cm}^{-3}$. n_0 for sample 1 and 7 were not measured but they were given similar values considering the n_0 of sample 5 and other carrier concentration measurements [1, 2, 3]. The evaluation of the electron(hole) binding energy $E_{T1}(E_h)$ was based on the analysis of the PL exponential thermal decay as follows. Assuming that the excitonic PL thermal quenching is caused by the thermal depopulation of the electron-attractive impurity centers T_1, the activation energy of the quenching process E_{qx} should be approximately equal to the electron binding energy of the center E_{T1}. The small energy difference between the two values should be equal to the hole binding energy E_h considering that $E_{T1} + E_h = E_g^{ind} - E_{ex} = E_{qx}$. In fact, inserting the following values: $E_{T1} \approx E_{qx}$, n_0, N_C and $g_{T1} = 1$ into Eq. 1.24 will yield a temperature evolution of the occupation probability similar to the integral PL thermal quenching occurring in all three samples. For $T < 50$K the occupation probability is equal to one, then as the temperature rises between 50K and 100K, the Fermi-level passes through the T_1 level and f_{T1}^e decreases by many orders of magnitude. The similar temperature evolution of the integral PL and the occupation probability confirms what was previously assumed: the thermalization of the electron-attractive centers leads to the dissociation of the bound excitons and to the quenching of the excitonic PL. This similar temperature behavior also helped in determining the values of E_{T1} and E_h for all three samples.

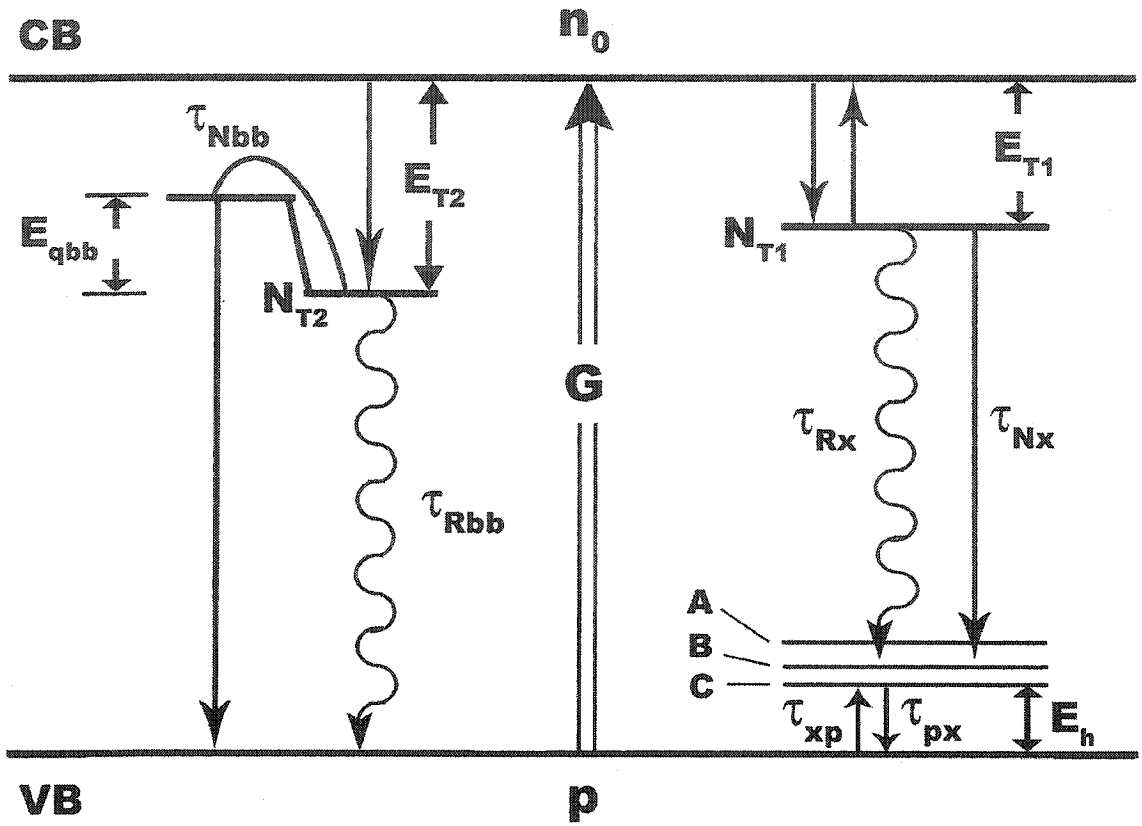

Figure 3.13: Zone diagram describing the kinetics of the excitonic (T_1) and broad-band (T_2) radiative channels.

τ_{Rbb} and τ_{Nbb} were determined with the τ_{Rbb}/τ_{Nbb} ratio given in Table 3.3 and with the following relation, derived from $E = hf$ in the case of a strong electron-phonon coupling:

$$\tau_{Nbb} \approx h/P_{bb} \tag{3.6}$$

where P_{bb} is the energy of the main phonon mode and h is Planck's constant. τ_{Rbb} and τ_{Nbb} were evaluated for samples 1 and 5 however similar values had to be estimated for sample 7 since $P_{bb}^{(7)}$ could not be determined experimentally. Finally τ_{Nx} was adjusted in to obtain the best fit with the experimental data. The kinetics of the the two-channel model is represented by the zone diagram in Figure 3.13. All the parameter values are displayed in Table 3.5.

	MoS_2 sample 1	WS_2 sample 5	WSe_2 sample 7
τ_{Rx} (Eq. 3.3)			
$\tau_{A,B,C}$	section 3.5.1	section 3.5.1	section 3.5.1
$g_{A,C}$	1	1	1
g_B	2	2	2
τ_{cp} (Eq. 1.22)			
ν_{th}			
m_h[1]	–	–	–
σ_{px}	1×10^{-16}	1×10^{-17}	1×10^{-17}
N_{T1}^e			
N_{T1}	1×10^{15}	1×10^{15}	1×10^{15}
g_T	1	1	1
n_0	1×10^{10}	1×10^{11}	1×10^{13}
E_{T1}	.090	.099	.058
N_C			
m_e[1]	–	–	–
τ_{xp} (Eq. 1.26)			
E_h	.026	.026	.026
σ_{px}	1×10^{-16}	1×10^{-17}	1×10^{-17}
m_h[1]	–	–	–
N_V			
m_h[1]	–	–	–
τ_{Nx}	1×10^{-5}	1×10^{-4}	1×10^{-6}
τ_{Rbb}	$\sim 1 \times 10^{-6}$	$\sim 1 \times 10^{-6}$	$\sim 1 \times 10^{-6}$
τ_{Nbb}	$\sim 3 \times 10^{-14}$	$\sim 3 \times 10^{-14}$	$\sim 3 \times 10^{-14}$

[1] From ref. [57, 58, 59], $m_e = m_h = m_0$ (m_0 is the free electron mass)

Table 3.5: Equation 1.20 and 1.21 Parameters

Discussion of the Model

Figure 3.14 presents the theoretical curves from Eqs. 1.20 and 1.21 as well as the the experimental data points of the excitonic and broad-band total integral PL intensity ($I_{ex}(T)$ and $I_{bb}(T)$) for samples 1, 5 and 7. The figure also illustrates the integral PL intensity of each individual excitonic lines A,B and C. The kinetic recombination model is in good agreement with the experimental measurements(All three fits have low chi square values) and, in contrast to the Mott-Seitz formula (Eq. 1.12) from section 3.2.2, accurately describes the temperature behavior of the integral PL intensity for low temperatures.

The abrupt increase of $I_{ex}(T)$ at 2 <T< 7K for sample 1 is caused by the long radiative decay life-time of the A-line compared to the B-line (measured as a ratio in section 3.5.1). This condition is very similar to the allowed and dipole-forbidden transitions of the excitonic doublet caused by the electron-hole j-j coupling described previously in section 3.4. At the lowest temperature the PL spectrum is dominated by the A-line and thus τ_{Rx} is determined by the long life-time τ_A. As the temperature rises, the thermal population of the short life-time B state leading to the appearance of the B-line and the reduction of the A-line in the PL spectra (the A-line disappears extremely rapidly and could not be measured accurately above 4.2K) dramatically increases simultaneously the radiative recombination efficiency and the $I_{ex}(T)$ observed in the 2K to 20K range (as seen in Figure 3.14, the influence of the C state in this temperature range in negligible). Further temperature increases lead to the population of the upper C state (with the shortest radiative life-time) leading to a relatively constant total radiative recombination efficiency between 20K and 55K before the thermal quenching process occurs.

Samples 5 and 7 also have similar temperature behaviors as sample 1. An increase of the $I_{ex}(T)$ at low temperature is once again observed in both samples however, due to the smaller life-time ratio between the A and B states as opposed to sample 1, the increase is smaller in sample 7 and smaller still in sample 5 (once again the C state contribution to the PL intensity in that temperature range is negligible for both samples). Increasing once again the temperature will thermally populate the short life-time C state which will contribute to the $I_{ex}(T)$ much like in sample 1. The intensity redistribution from the A-line to the B-line as the temperature increases can be observed quite clearly in Figure 3.14 for sample 5 and 7 as opposed to sample 1. An increase of the integral PL intensity of both A and B levels for $T > 10$K is observed uniquely in sample 7. This increase can be attributed to the simultaneous thermal population of the A and B states due to the very small energy separation between them. Sample 5, having a higher energy

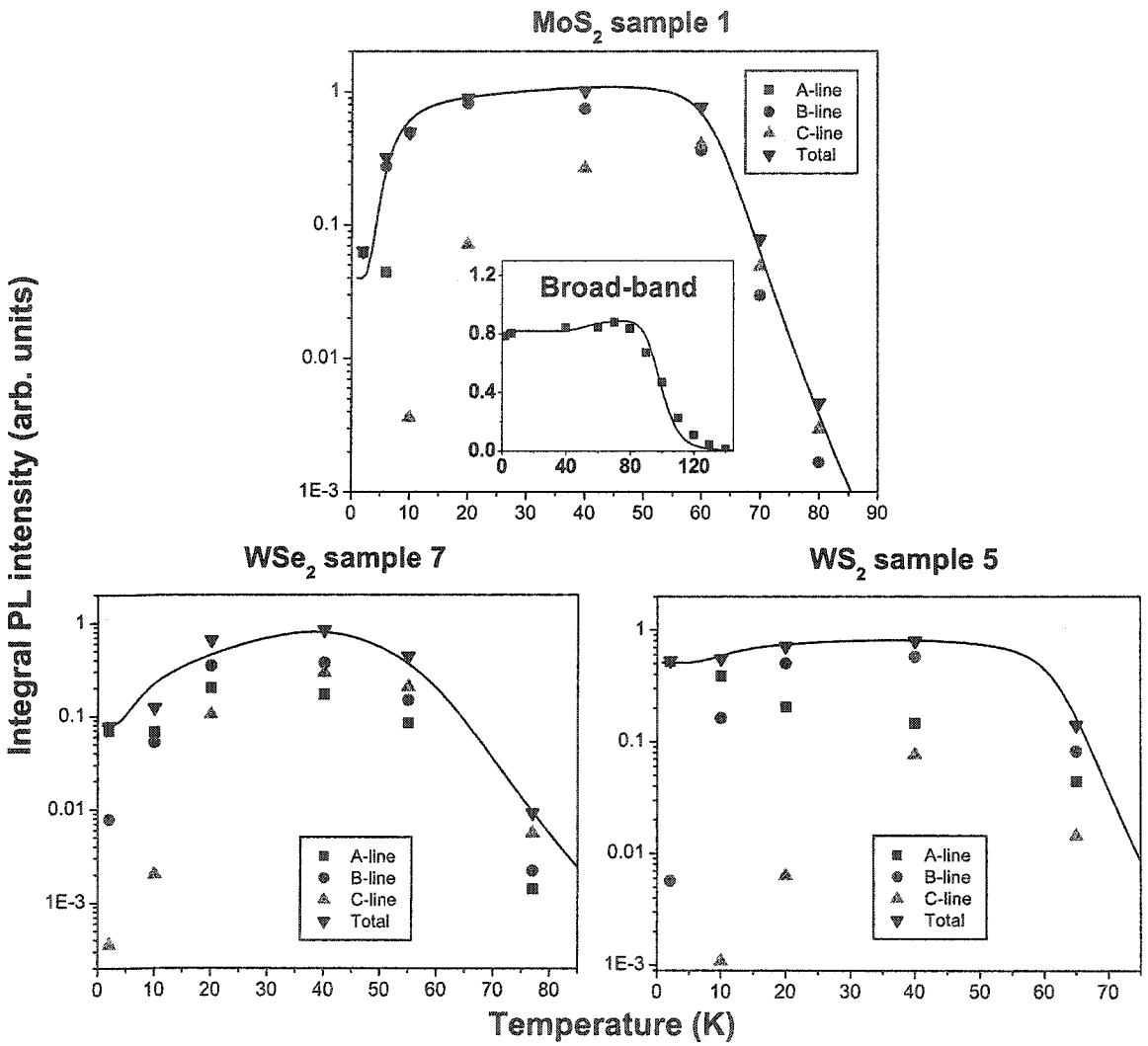

Figure 3.14: Fit of Eqs. 1.20 and 1.21 to the total integral PL intensities for samples 1, 5 and 7. The integral PL intensity for each individual lines (A,B and C) are also depicted.

difference between lines A and B, did not show such an increase. The A-B integral PL intensity redistribution can also be observed in sample 1 at very low temperatures; however because of the enormous difference between the two radiative recombination rates, the redistribution effect is quite small.

The experimental broad-band $I_{bb}(T)$ temperature evolution is also well described by the recombination model. The intensity of the broad-band emission does not depend on the excitonic recombination efficiency; the quenching of the band takes place only when the sharp lines have totally vanished. This indicates that the recombination rate via the broad-band channel is much higher than that via the excitonic one. Therefore, as stated previously, the radiative recombination caused by the deep level can be treated as a shunt channel for the excitonic PL intensity. A slight increase of the $I_{bb}(T)$, previously mentioned in section 3.2.2 and now illustrated more accurately in Figure 3.14, is observed between the excitonic and broad-band thermal quenching temperatures. This increase is due to the extra carriers from the thermalized T_1 centers now recombining radiatively through the deep centers T_2.

Although the recombination model describes very well the temperature evolution of the excitonic and broad-band integral PL intensities of the samples at low temperatures, it does not take into account donor acceptor pair contributions at higher temperatures and ultimately fails beyond $T \approx 100$K. Other small inconsistencies arising between the model and the experimental results originate mostly from taking experimentally measured parameter values from a particular sample and assigning them to other samples.

3.5.3 Configuration Coordinate Diagram

Figure 3.15 illustrates a configuration coordinate diagram for the MoS_2 sample 1. Although the kinetic recombination model shown in Figure 3.13 accurately illustrates the kinetics of the radiative and nonradiative processes of the T_1 and T_2 channels, the CCD introduced in section 1.4.3 was constructed in order to more effectively describe the interactions between the electronic and vibronic transitions of the deep center T_2. The energy values E_{bb}, E_{qbb}, Δ_{bb}, E_g^{ind} in addition to the MoS_2 E_{LO} [40] and P_{bb} phonon energies, assumed to correspond to the vibrational quanta of the carrier in the free (ground) and trapped (excited) states, were used to calculate the potential energy curves of the deep center T_2 and of the indirect band gap, described by Eqs. 1.27 and 1.28 respectively, in the frame of the semiclassical approximation [30].

The potential energy curve for the halogen molecule trap T_1 was also calculated. As

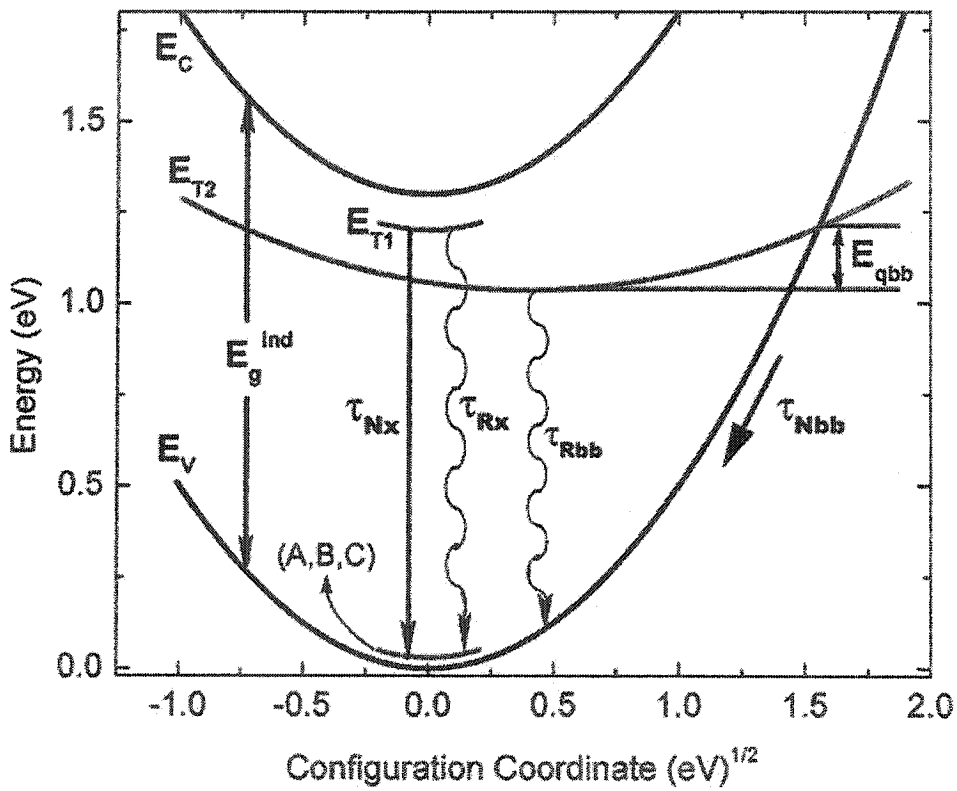

Figure 3.15: Configuration coordinate diagram of MoS_2 sample 1.

mentioned in section 3.4.3, the thermal quenching of the excitonic luminescence is not caused by a nonradiative multiphonon recombination process but rather by the thermalization of the the impurity center T_1. The curve therefore disappears beyond $\pm \sqrt{E_{qx}/2}$ and does not cross any other potential energy curves. Furthermore, considering the weakness of the electron-phonon coupling inherent in isoelectronic centers as opposed to deep centers (typical value of the Huang-Rhys factor $S = 0.2 - 0.3$ [29, 63]), the T_1 potential energy curve was positioned with a zero offset relative to the indirect band gap.

3.6 PL versus intensity and excitation geometry

Measurements of the bound exciton PL as a function of excitation intensity and excitation geometry were performed on some MoS_2 and WS_2 synthetic crystals. Data acquisition of the dependence of the PL as a function of Intensity for MoS_2 sample 1 and 3, illustrated in Figure 3.16, was performed at constant temperature $T = 2K$. The maximum power of the laser was 80 mW. No changes were observed in the PL spectra confirming that no temperature increase occurred during the measurements. The experimental data was fitted by the following simple power law:

$$I \propto L^{\gamma} \tag{3.7}$$

where I is the total ZPL integral PL intensity (at $T = 2K$ the PL was comprised of the A line only), L is the excitation laser intensity and γ is a dimensionless exponent representing the ratio between the number of excitonic radiative recombination and the number of electron-hole pairs created. Both samples demonstrated a sublinear dependence of $\gamma = 0.608$ for sample 1 and $\gamma = 0.730$ for sample 3. This type of power dependence is a common behavior for bound exciton recombination [64]. Due to the small number of impurities in the samples, an increase in excitation intensity eventually leads to the saturation of the radiative centers, and a limit of the number of radiative recombination possible is reached. Therefore it can be concluded that sample 3, having a higher γ than sample 1, has a greater concentration of halogen molecules intercalated between its layers. A sublinear power dependence was also observed in WS_2 sample 5 as shown in Figure 3.16 inset.

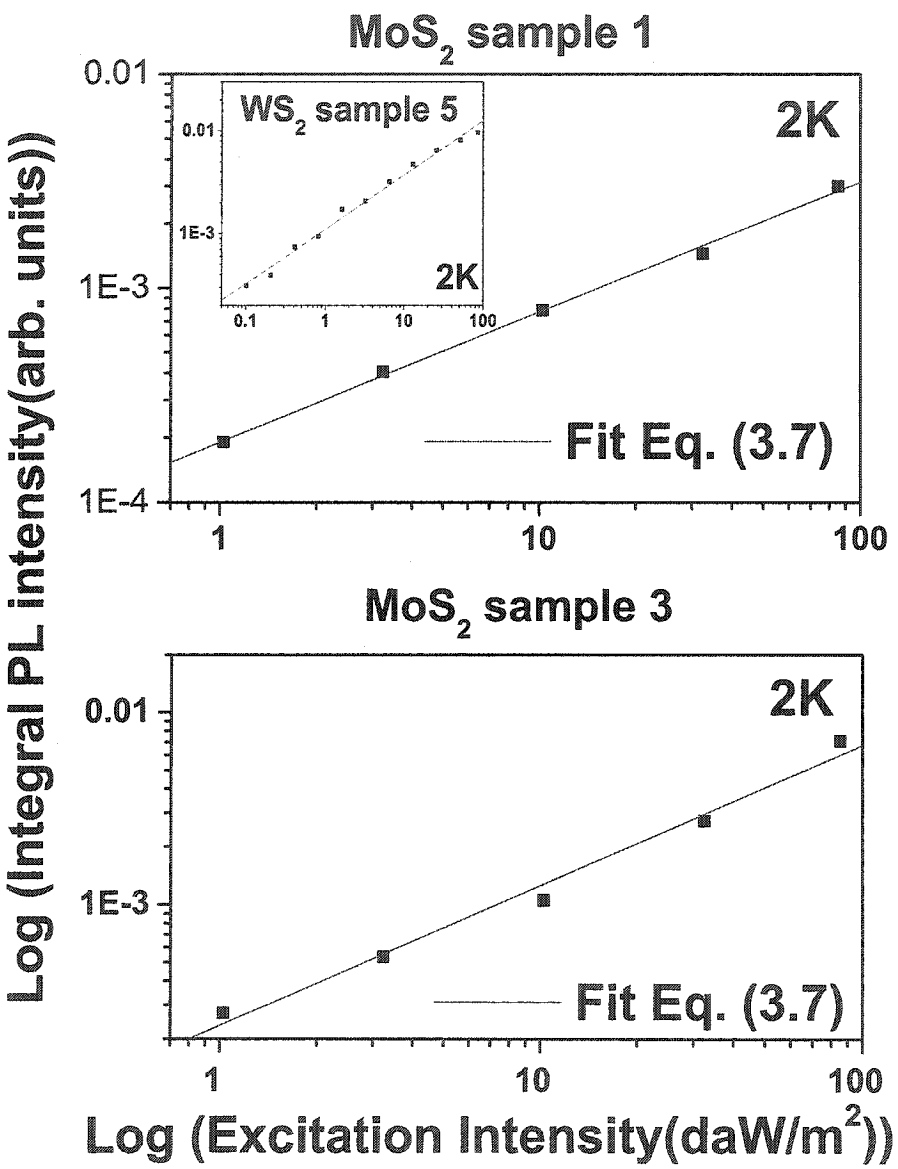

Figure 3.16: Integral PL intensity dependence on excitation intensity for sample 1 and 3 and 5 at 2K.

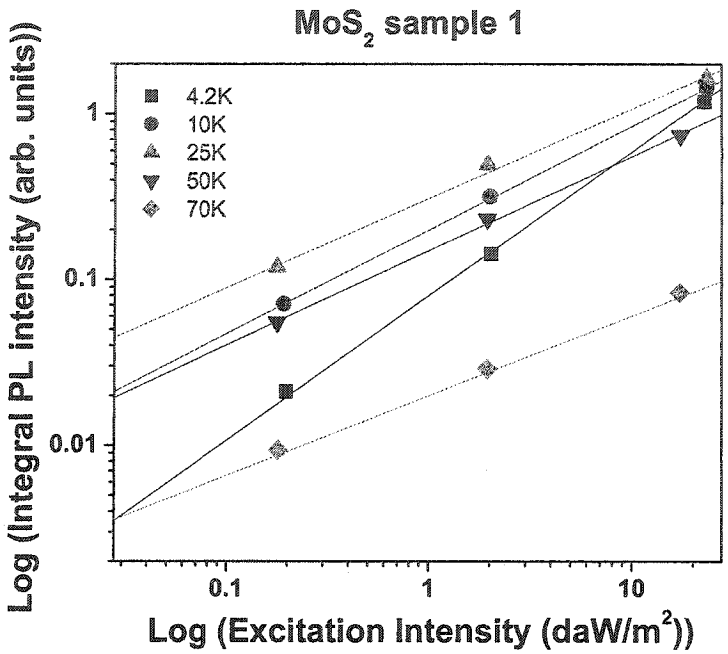

Figure 3.17: Integral PL intensity dependence on excitation intensity for sample 1 at various temperature.

The excitonic PL versus excitation intensity of sample 1 was also measured at various temperatures. The maximum power of the exciting laser was 20 mW. The data was once again fitted with Eq. 3.7 where a temperature dependence of the slope (γ) was revealed (see Figure 3.17). As observed in Figure 3.18, γ initially decreases very rapidly before levelling off at approximately $T = 30K$ and then start to decrease once more at $T > 50$K. This evolution can be easily explained with a closer investigation of the temperature dependent integral PL intensity of each individual ZPLs depicted in Figure 3.18 inset. A decreasing γ at low temperatures, where the B line is dominant, (line A was neglected due to its minor contribution to the integral intensity in this temperature range in comparison to B) suggests an initial partial saturation of the radiative centers. The ever increasing population of the B level as the temperature rises is ineffective in compensating for the increasing number of electron-hole pairs available for the centers therefore γ continues to decline. At $T \approx 50$K the C level begins to fill therefore increasing the number of radiative recombination and consequently slightly increasing γ. Finally, the thermalization of the impurity centers occurs at higher temperatures and γ decreases once again.

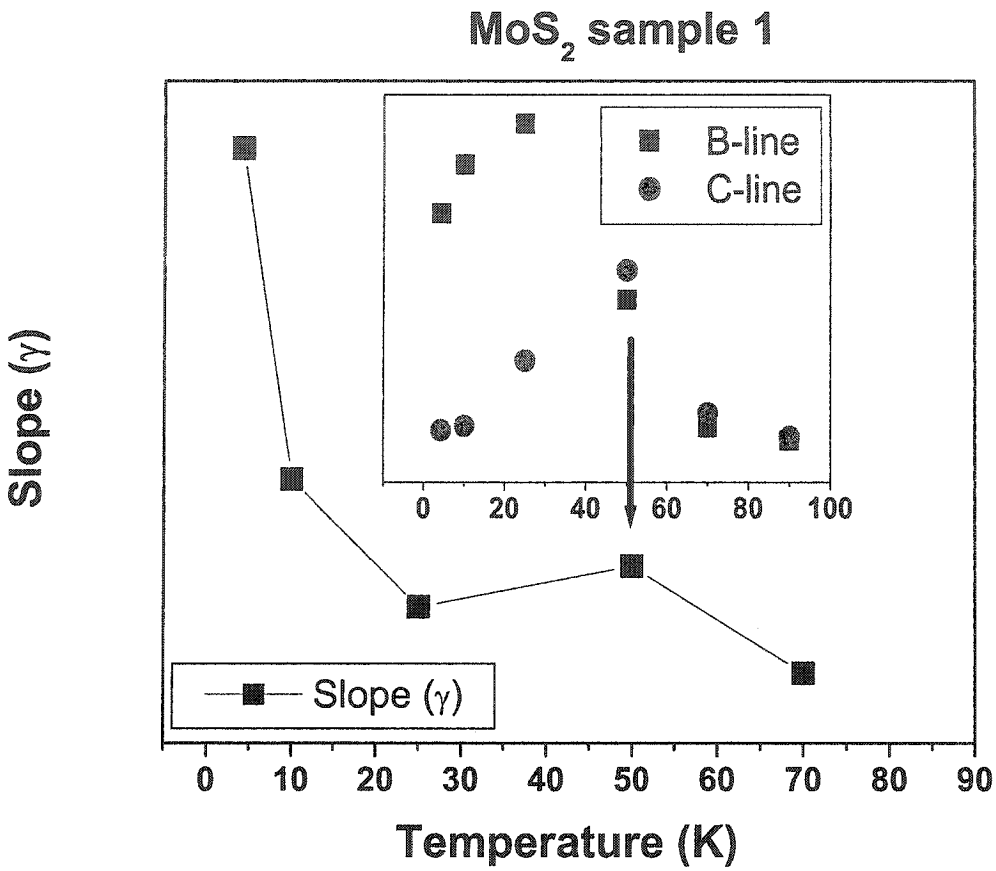

Figure 3.18: Temperature dependence of the slope (γ) for sample 1. The inset presents the integral PL intensity of the B and C lines as a function of temperature. The line connecting the experimental data points is a visual aide only.

The excitonic PL intensity of the samples was also investigated for the two excitation geometries seen in Figure 2.1 inset. While no spectral differences were observed in the PL spectra taken in the two geometries, the PL signal parallel to the layers was greater than the signal measured perpendicular to the layers (up to 5 times greater). This increase, observed for all MoS_2 and WS_2 synthetic samples, occurs perhaps because the PL signal is not attenuated going along the layers.

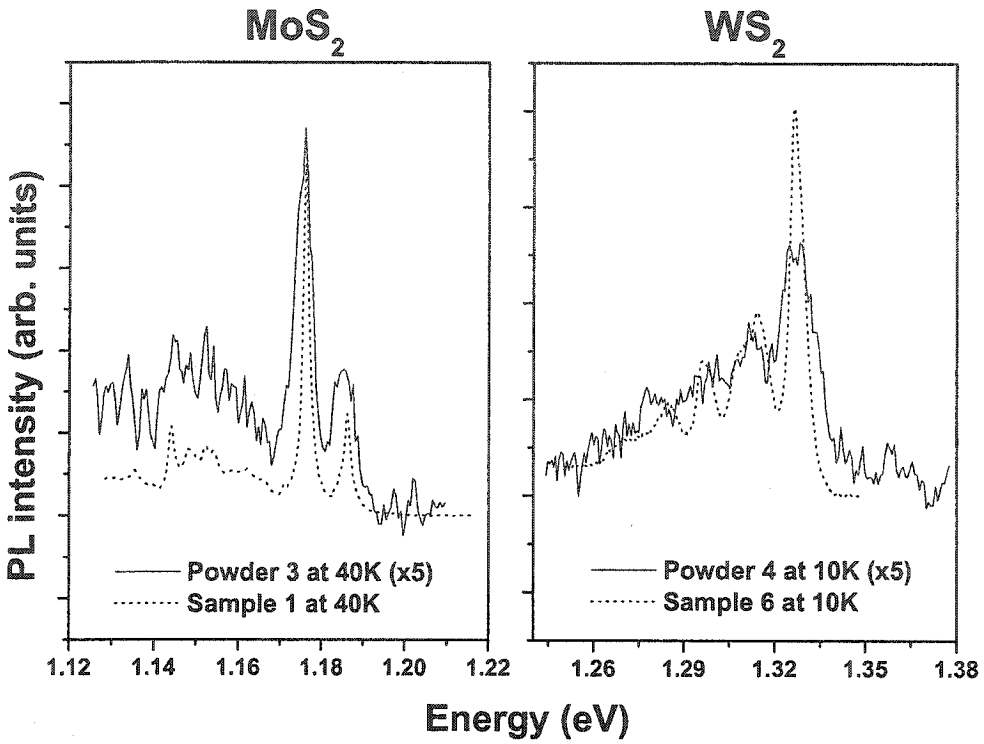

Figure 3.19: PL spectra comparison between powders and synthetic single crystals.

3.7 Photoluminescence of powders and Intercalation processes

3.7.1 Powders

In addition to synthetic and natural single crystals, spectral measurements were also performed on very fine grained commercial WS_2 and MoS_2 powders. The PL measurements on the purchased synthetic WS_2 powder (powder 4) exhibited radiative emission in the same range as the synthetic single crystals sample 5 and 6. A comparison of the PL spectra at various temperatures of the powder (fabrication process unknown) and single crystals revealed a good agreement between the PL from the synthetic crystal grown with iodine and the powder, suggesting the two samples were grown with the same transport agent (see Figure 3.19).

The *natural* commercial MoS_2 powders (powder 1, 2 and 3) also displayed the same bound exciton recombination luminescence as the synthetic single crystals (samples 1, 2 and 3) and therefore going against the initial assumption that only the synthetic single

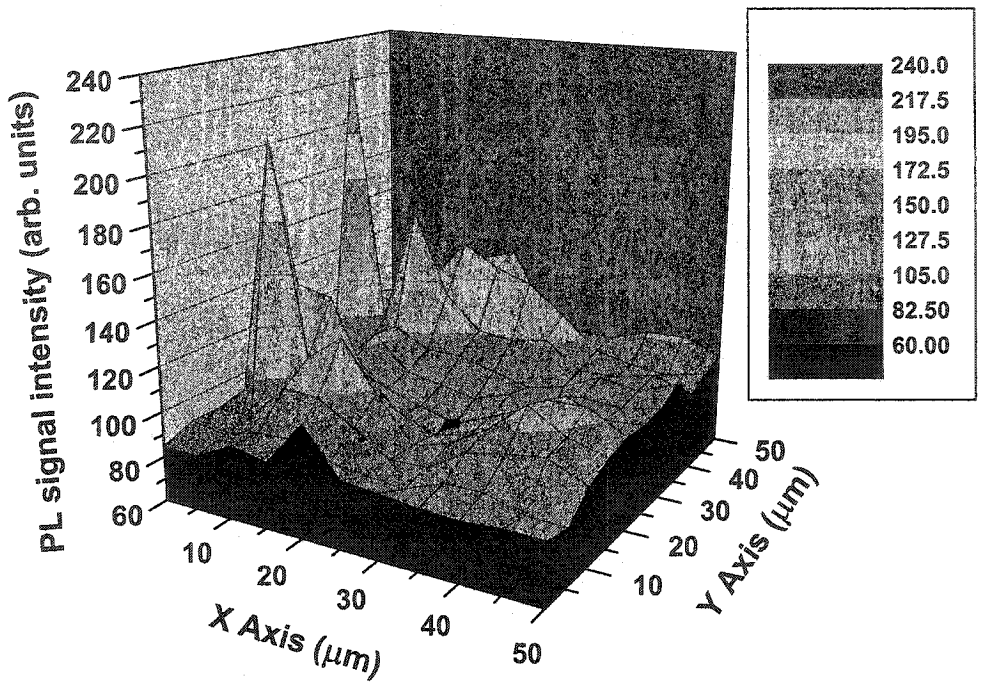

Figure 3.20: 2D mapping of the PL intensity from a $50 \times 50\mu$m area on powder 3.

crystals grown with halogen transport agent could exhibit such radiative properties. The PL emissions of powder 3 and sample 1 are compared in Figure 3.19. It was established that the commercial powders underwent heat treatments in a chlorine atmosphere in order to purify the molybdenite, a common practice in the recovery ore processing [65]. A chemical analysis was performed at SGS Lakefield research and confirmed the presence of chlorine in all three powders in the following amounts: 36 ppm for powder 1, 41 ppm for powder 2 and 56 ppm for powder 3. This indicated that the intercalation of halogen molecules between the layers of MoS_2 does not only occur during the crystal growth process but may also be induced in natural molybdenite.

As mentioned in section 2.1.2, the powders were compressed into small pellets in order to perform PL measurements. The intensity of the PL was extremely sensitive to the position and angle of excitation on the MoS_2 and WS_2 powder samples. Typical intensities were approximately five times lower than the synthetic samples however, depending on the angle or position. Figure 3.20 illustrates a mapping of the B-line PL intensity of the MoS_2 powder 3 in an area of 50×50 microns at a fixed temperature of 4.2K. The experiment was performed at the NRC using a special optical cryostat mounted on a

motorized platform. The frequency-doubled cw diode pumped YAG laser beam(532 nm) used for the excitation source was focused on the sample with a microscope objective. The spot size diameter of the beam was approximately a few microns. The luminescence was then collected by a CCD (charge coupled device) detector. The observed PL intensity anisotropy from Figure 3.20 is believed to originate from the local grain orientation. As seen in section 3.6, higher PL intensities were measured depending on the orientation of the single crystal. For this reason it is possible that a similar effect could occur on a more local scale in the powders.

3.7.2 Intercalation of natural single crystals

Based on the heat treatment techniques in [65] and numerous crystal growth methods using halogen transport agents [48, 49, 50, 66] , several experiments described in section 2.4 were initiated in an attempt to intercalate halogen molecules within the layers of natural MoS_2 single crystals. Applying the same conditions as the heat treatment performed on the commercial powders (300 Celsius in a chlorine atmosphere), natural MoS_2 single crystals were heated for four days. Subsequent PL measurements on the treated sample revealed a very faint infrared signal, suggesting a possible chlorine intercalation had occurred. Figure 3.21 illustrates the PL spectra of the synthetic and natural MoS_2 single crystals for two different temperatures. Although the PL intensity of the treated natural single crystals was approximately 20 times lower than that of the synthetic crystals, it displayed the same ZPLs and a similar PL temperature evolution indicating that the intercalation of halogen molecules had occurred within the natural single crystal.

Trials to intercalate bromine and iodine into natural MoS_2 single crystals were also conducted but did not yield any results. These failures could possibly be related to the size of the halogen molecules compared to the inter-layer spacing of the host lattice. As seen in section 3.4 the only halogen molecule small enough to enter the van der Waals space is chlorine, both iodine and bromine are simply too large. However, all three molecules can still be intercalated *during* the growth process as the layers form one over the other.

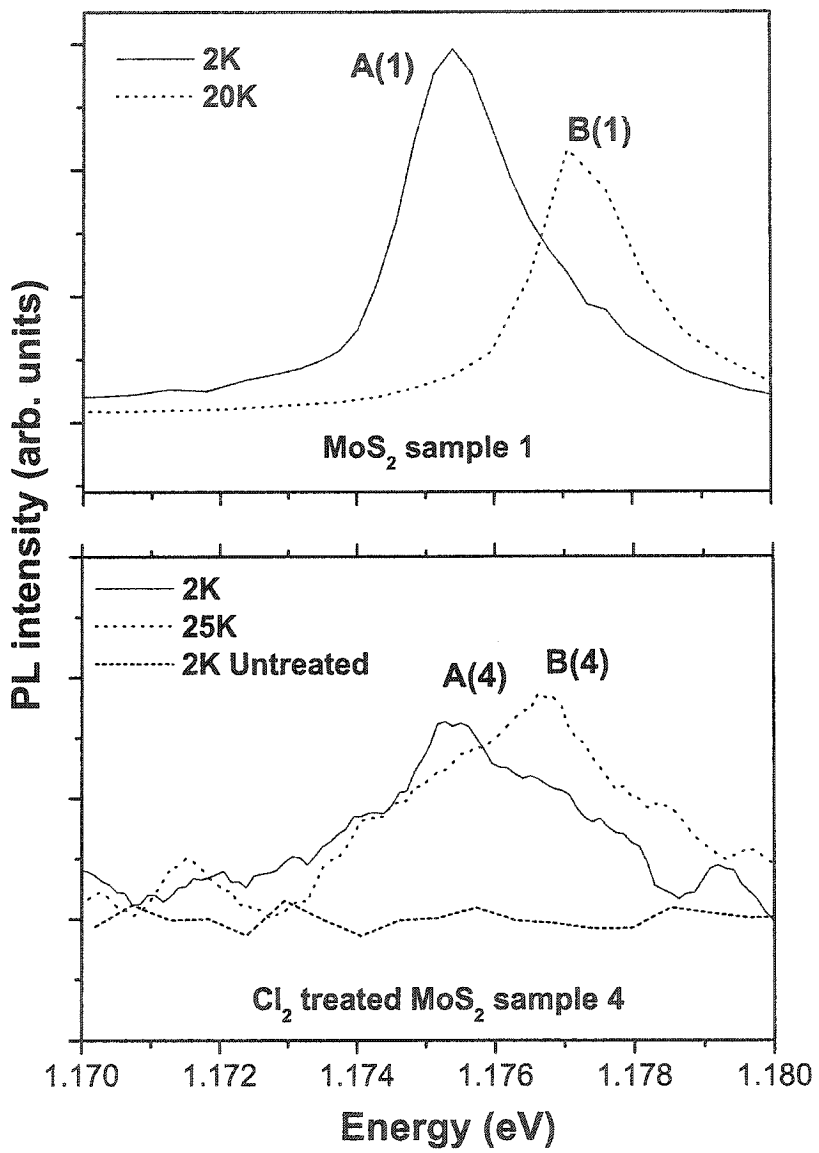

Figure 3.21: PL spectra of the synthetic MoS_2 single crystal sample 1 and the chlorine treated natural MoS_2 single crystal sample 4 at two temperatures. The 2K PL spectrum of an untreated natural MoS_2 crystal is also shown.

The lower PL intensity of the treated natural MoS_2 single crystal as opposed to the synthetic material($\sim$ 20 times lower) and to the natural powder ($\sim$ 15 times lower) is most likely associated to a very low concentration of halogen molecules intercalated in the natural single crystal sample. Although the time during which the natural powders are exposed to the Cl_2 heat treatment is unknown, it is expected to be no longer than a few days. Such a dramatic difference in PL intensity between the natural powders and single crystals is speculated to be caused by the small grain size of the powders. The grains would possibly have a greater effective area where the halogen impurities can enter between the layers and thus might be more easily intercalated than the larger natural single crystals. Consequently, a longer intercalation time would be needed for a natural single crystal sample to obtain the same halogen concentration as in an equivalent powder sample. It is clear that more research on the concentration of halogens in synthetic crystals, natural powders and treated single crystals as well as the intercalation time is needed to fully understand and quantify the halogen intercalation process.

Conclusion

The present research was undertaken to study the newly discovered radiative properties exhibited in the transition metal dichalcogenide MoS_2, WS_2 and WSe_2 layered compounds. The PL characteristic spectra from the synthetic single crystals of all three materials obtained from steady-state PL measurements revealed two distinct radiative regions: the excitonic and broad-band regions. While the broad-band region was observed in all synthetic and natural single crystals, the excitonic region was initally seen exclusively in the synthetic single crystals grown by vapor transport method with halogens as the transport agent.

Through a series of PL measurements taken between 2K and 150K, the temperature dependence of the spectral structure and radiative intensity of both regions was studied. The excitonic region of the three compounds displayed three major zero-phonon lines (A,B and C) from which the PL intensity redistribution was played out. The spectral structure of the broad-band region in the sythetic MoS_2 single crystal remained relatively the same with the exception of the phonon peaks gradually fading with increasing temperature. A thermal quenching process was also observed for both regions. The energy difference between the activation energies of the excitonic and broad-band quenching suggested two distinct quenching mechanisms.

Time-resolved measurements on one of the WS_2 synthetic crystals was also presented. The temperature evolution of the decay time was explained with a multi-level time-decay model. Since time-resolved measurements were not or could not be performed on the MoS_2 and WSe_2 synthetic samples, information on the decay times for these compounds was extracted via integral PL intensity ratios of the excitonic states.

After the steady-state PL measurements were presented, the origin of both radiative regions was then studied thoroughly. The excitonic region was attributed to the radiative recombination of excitons bound to neutral centers, similar to those present in isoelectronically doped GaP and Si semiconductors. An in depth analysis of the lattice structure using geometrical calculations, PC measurements of the synthetic MoS_2 and

WS_2 single crystals and finally the abscence of excitonic PL in the natural MoS_2 single crystals and in WSe_2 grown without halogen transport agent, all confirmed that the impurity centers were formed by the diatomic halogen molecules intercalated within the van der Waals gaps of the layered materials. In the case of the broad-band region, the spectral emissions were associated to radiative transitions between deep donor centers, arising from intrinsic lattice defects, and the valence band in the conditions of a strong electron-phonon coupling. The two distinct thermal quenching mechanisms of both radiative regions were also identified. While the bound exciton states in the MoS_2, WS_2 and WSe_2 compounds do resemble the ones in GaP and Si, it is still uncertain if they actually come from an electron-hole *j-j* coupling. Zeeman effect measurements would confirm the origin of the excitonic multiplets.

Next, a kinetic recombination model was suggested to describe the temperature evolution of the integral PL intensity of both radiative regions simultaneously. The model proposed was composed of two separate radiative channels: a bound exciton radiative recombination channel and a shunt path. The excitonic region PL quenching occurred due to the thermal depopulation of the impurity centers while the broad-band PL quenching was caused by a nonradiative multiphonon recombination channel becoming available at higher temperatures. Using the information gathered from the steady-state PL and time-resolved measurements, the model was fitted to the MoS_2, WS_2 and WSe_2 synthetic crystals experimental data. The model described the integral PL intensity temperature behavior however, since it did not consider donor acceptor pair contributions, the model ultimately failed at temperatures above $T \approx 100$K. The small discrepancies between the experimental data and the theoretical curves originated mostly from taking experimentally measured parameter values of particular samples and assigning them to different samples.

A preliminary study on the PL intensity dependence on the synthetic MoS_2 and WS_2 single crystals was performed and showed the sublinear behavior of the bound exciton recombination as well as its dependence on temperature. It was also observed that different concentrations of halogen molecules in the synthetic MoS_2 may have been achieved during the growth process (possibly related to the initial quantity of transport agent).

Steady-state PL measurements performed on the commercial MoS_2 natural powders revealed the same excitonic region as the synthetic single crystals suggesting that the intercalation of halogen molecules could be achieved in some other way than during the crystal growth process. The intercalation of the chlorine halogen molecules within the

natural MoS_2 single crystals confirmed the assumption.

While the basic underlying properties of this newly discovered optical phenomenon has been documented, much work remains to be done. Several other transition metal dichalgonides layered semiconductors such as $MoSe_2$ and $MoTe_2$ grown with halogen molecules are also expected to exhibit similar radiative properties and should be investigated. A more quantitative study of halogen concentration effects on the PL of single crystals and powders could also be potentially studied. The intercalation of layered compounds with alkalis and other substances has been well documented over the years [12, 16] yet no IR radiative emissions have been observed and could therefore also be researched. The ever growing field of nanotechnology could also offer new and interesting venues of research, such as studying possible radiative properties of synthesized MoS_2 and WS_2 nanotubes grown with halogens [68, 69] as was recently done for carbon nanotubes[67]. In conclusion, we hope that the work presented in this thesis will rekindle the interest and encourage more research on the transition metal dichalcogenides.

Bibliography

[1] J.A. Wilson and A.D. Yoffe, Adv. Phys. **18**, 193 (1969).

[2] S.W.H. El-Mahalawy and B.L. Evans, Phys. Status Solidi B **79**, 713 (1977).

[3] A.J. Grant, T.M. Griffith, G.D. Pitt, and A.D. Yoffe, J. Phys. C **8**, L17 (1975).

[4] T. Böker, R.Severin, A. Müller, C. Janowitz, R. Manzke, D. Vob, and P. Krüger, Phys. Rev. B **64**, 235305 (2001).

[5] A. Klein, S. Tiefenbacher, V. Eyert, C. Pettenkofer, and W. Jaegermann, Phys. Rev. B **64**, 205416 (2001).

[6] S. Sharma, C. Ambrosh-Draxl, M.A. Khan, P. Blaha, S. Auluck, Phys. Rev. B **60**, 8610 (1999).

[7] *Photoelectrochemistry and Photovoltaics of Layered Semiconductors*, edited by A. Aruchamy (Kluwer Academic Publishers, Dordrecht, 1992).

[8] G. Kline, K.K. Kam, R. Ziegler, and B.A. Parkinson, Sol. Energy Mater. **6**, 337 (1982).

[9] G.L. Frey, S. Elani, M. Homoyonfer, Y. Feldman, and R. Tenne, Phys. Rev. B **57**, 6666 (1998).

[10] R. Tenne, L. Margulis, M. Genut, and G. Hodes, Nature (London) **360**, 444 (1992).

[11] G. Seifert, H. Terrones, G. Jungnickel, and T. Frauenheim, Phys. Rev. Lett. **85**, 146 (2000).

[12] *Intercalated Layered Materials*, edited by F. Lévy (D. Reidel Publishing Company, Dordrecht, 1979)

[13] R.B. Somoano and A. Rembaun, Phys. Rev. Lett. **27**, 402 (1971).

[14] A.H. Reshak, S. Auluck, Phys. Rev. B **68**, 125101 (2003).

[15] A.H. Reshak, S. Auluck, Phys. Rev. B **68**, 195107 (2003).

[16] E. Benavente, M.A. Santa Ana, F. Mendizàbal, G. González, Coord. Chem. Rev. **224**, 87 (2002).

[17] Y.V. Zubavichus, A.S. Golub, N.D. Lenenko, Y.N. Novikov, Y.L. Slovokhotov, M. Danot, J. Mol. Cat. A: Chemical **158**, 231 (2000).

[18] R.H. Friend, A.D. Yoffe, Adv. Phys. **36**, 1 (1987).

[19] L. Kulyuk, E. Bucher, L. Charron, E. Fortin, A. Nateprov, and O. Schenker, Nonlinear Optics **29(7-9)**, 501 (2002).

[20] L. Kulyuk, L. Charron, and E. Fortin, Phys. Rev. B **68**, 075314 (2003).

[21] *Introduction to Semiconductor Optics*, N. Peyghambarian, S. W. Koch, A. Mysyrowicz, Prentice Hall, New Jersey (1993)

[22] P.J. Dean and D.C. Herbert, *Excitons*(Springer, New York, 1979), Vol. 14.

[23] Y. Toyozawa, S.S. Electronics **21**, 1313 (1978)

[24] *Luminescence in Solids*, ed. D.R. Vij, Plenum Press, New York (1998).

[25] P. Bergman, B. Monemar, M.-E. Pistol, Phys. Rev. B **40**, 12280 (1989).

[26] P.D. Dapkus, W.H. Hackett Jr., O.G. Lorimor, R.Z. Bachrach, J. Appl. Phys. **45**, 4920 (1974).

[27] *Semiconductor Statistics*, J.S. Blakemore, Pergamon Press, Oxford (1962).

[28] J.S. Jayson and R.Z. Bachrach, Phys. Rev. B **4**, 477 (1971).

[29] Y. Zhang, W. Ge, M.D. Sturge, J. Zheng, and B. Wu, Phys. Rev. B **47**, 6330 (1993).

[30] D. Curie, in *Optical Properties of Ions in Solids*, edited by B. di Bartolo (Plenum Press, New York, 1975).

[31] Y. Marfaing, in *Handbook on Semiconductors: Optical Properties of Solids*, edited by M. Balkanski (North-Holland Publishing Company, Amsterdam·New York·Oxford, 1980).

[32] S.K. Srivastava, B.N. Avasthi, J. Mat. Sci. **20**, 3801 (1985).

[33] E. Fortin and F. Raga, Phys. Rev. B **11**, 905 (1975).

[34] E. Fortin and W.M. Sears, J. Phys. Chem. Solids **43**, 881 (1982).

[35] E. Arushanov,E. Bucher, K. Friemelt, O. Kulikova, L. Kulyuk, A. Nateprov, A. Siminel, Proc. 19th Int. Semicond. Conference CAS-96, Romania (1996).

[36] A. Jaegerwaldau, E. Bucher, Thin Solid Films **200**, 157 (1991).

[37] C. Sourisseau, F. Cruege, M. Fouassier, Chem. Phys. **150**, 281 (1991).

[38] A.M. Stacy and D.T. Hodul, J. Phys. Chem. Solids **46**, 405 (1985).

[39] T.J. Wieting and J.L. Verble, Phys. Rev. B **3**, 4286 (1970).

[40] S. Uchida and S. Tanaka, J. Phys. Soc. Jpn. **45**, 153 (1978).

[41] W. Czaja, Festkoerperprobleme **11**, 65 (1971).

[42] X. Zhang, K. Dou, Q. Hong, and M. Balkanski, Phys. Rev. B **41**, 1376 (1990).

[43] L. Merz, R.A. Faulkner, and P.J. Dean, Phys. Rev. **188**, 1228 (1969).

[44] J. Weber, W. Schmid, and R. Sauer, Phys. Rev. B **21**, 2401 (1980).

[45] M. Godlewski, W.M. Chen, M.E. Pistol, B. Monemar, and H.P. Gislason, Phys. Rev. B **32**, 6650 (1985).

[46] B. Gil, M. Baj, J. Camassel, H. Mathieu, C.B. la Guillaume, N. Mestres, and J. Pascual, Phys Rev. B **29**, 3398 (1984).

[47] W. Jaegermann, Ber. Bunsenges. Phys. Chem. **92**, 537 (1988).

[48] C. Piña, P. Bosch, D. Acosta, J. Barreto, A. Vazquez, E. Camarillo, J. Crys. Growth **96**, 685 (1989).

[49] D.M. D'Ambra, J.V. Marzik, R. Kershaw, J. Baglio, K. Dwight, A. Wold, J. Sol. Stat. Chem. **57**, 351 (1985).

[50] A.A. Al-Hilli, B. L. Evans, J. Crys. Growth **15**, 93 (1972).

[51] W.J. Schutte, J.L. de Boer, and F. Jellinek, J. Solid State Chem. **70**, 207 (1987).

[52] www.webelements.com

[53] T.J. Wieting, A.D. Yoffe, Phys. Stat. Sol. **37**, 353 (1970).

[54] C.H. Henry and D.V. Lang, Phys. Rev. B **15**, 989 (1977).

[55] D.V. Lang, in *Deep Centers in Semiconductors: A State of the Art Approach*, edited by S.T. Panteleides (Gordon and Breach, New York, 1992).

[56] J.D. Cuthbert, D.G. Thomas, Phys. Rev. **154**, 763 (1967).

[57] R. Coehoorn, C. Haas, R.A. de Groot, Phys. Rev. B **35**, 6203 (1987).

[58] J. Baglio, E. Kamieniecki, N. DeCola, C. Struck, J. Marzik, K. Dwight, A. Wold, J. Sol. Stat. Chem. **49**, 166 (1983).

[59] T. Finteis, M. Hengsberger, T. Straub, K. Fauth, R. Claessen, P. Auer, P. Steiner, S. Hüfner, Phys. Rev. B **55**, 10400 (1997).

[60] J. M. Dishman and M. DiDomenico Jr., Phys. Rev. B **1**, 3381 (1970).

[61] M. Sternheim and E. Cohen, Phys. Rev. B **22**, 1875 (1980).

[62] L. Kulyuk, K. Friemelt, S. Popov, J.H. Schön, E. Bucher, Unpublished

[63] H. Dai, M.A. Gundersen, C.W. Myles, and P.G. Snyder, Phys. Rev. B **37**, 1205 (1988).

[64] S. Ghosh, J. Weber, H. Presting, Phys. Rev. B **61**, 15625 (2000).

[65] R.R. Dorfler, J.M. Laferty, JOM: Journal of Metals, May, 48 (1981).

[66] G.H. Yousefi, J. Mat. Sci. Lett. **9**, 1216 (1990).

[67] J. Lefebvre, Y. Homma, P. Finnie, Phys. Rev. Lett. **90**, 217401 (2003).

[68] M. Verstraete, J.-C. Charlier, Phys. Rev. B. **68**, 045423 (2003).

[69] S.-H. Jhi, S.G. Louie, M.L. Cohen, Sol. Stat. Comm. **123**, 495 (2002).